**ETH**zürich

PAUL SCHERRER INSTITUT

PSI

# Laser Stabilization for Manipulation of $^{40}$Ca$^+$ Ions

Master's Thesis

Yingying Cui

Trapped Ion Quantum Information group, ETH Zurich
Ion Trap Quantum Computing group, ETH Zurich - PSI Quantum Computing Hub

**Supervisors:**
Dr. Robin Oswald,
Dr. Jackson Ang'ong'a,
Dr. Cornelius Hempel,
Prof. Dr. Jonathan Home

June 2023

# Acknowledgments

The time for my master's thesis has been my favorite experience at ETH. The happiness truly comes from all the people I have been working with.

First, I would like to thank Robin Oswald. He is very knowledgeable about control engineering and has become my role model in research. He is also very patient and helpful. Most of the experiments and analyses in this thesis were done by us together. I will remember the days when he tutored me all day long with so much passion.

Second, I would like to thank Jackson Ang'ong'a. He has devoted significant time to teach me optics. From alignment techniques to 3D printing, I have acquired many useful skills. Working with him, I feel comfortable seeking his help whenever needed.

Next, I would like to thank Cornelius Hempel. His insightful comments on my lab notes have inspired me to think critically about my experiments. His recognition for me also encouraged me more towards research.

I also want to express my appreciation to Philip Leindecker and Edgar Brucke for their care and assistance throughout the project.

Finally, I would like to thank Jonathan Home for providing me with this amazing opportunity. Thank you for gathering all the great people around.

Thanks to everyone from the PSI team and TIQI group for their support.

# Abstract

The lasers used to manipulate $^{40}\text{Ca}^+$ ions in quantum computing experiments require frequency stability ranging from the MHz level for the dipole transitions down to the Hz level for the quadruple transition at 729 nm. While achieving the former is relatively straightforward, reaching the latter requires considerable effort. In this project, we lock various lasers to optical cavities using the PDH technique. We focus particularly on the two 729 nm laser systems based on a diode laser and a Ti:Sapphire laser respectively. We investigate what limits these feedback stabilization loops, and assess the practical consequences of these limits in terms of the achievable residual phase noise of the lasers.

# Contents

# 1 Motivation for Laser Frequency Stabilization

## 1.1 Introduction

Compared to classical computing, quantum computing possesses distinct features such as superposition and entanglement. Superposition enables the storage of an enormous amount of information, while entanglement allows for parallel operations. Quantum algorithms have therefore shown potentially exponential speedup over classical computers [21]. One method for quantum computing involves using ions as qubits, where quantum gates are executed through interactions with laser light [6].

Our group uses the charged particles $^{40}Ca^+$, confined in a radio-frequency trap (Paul trap), as a platform for quantum computing. The atomic structure of the Calcium ion is shown in Figure 2. The neutral Calcium atom undergoes a two-step photo-ionization: First, the laser at 423 nm puts one of the two valence electrons into an excited state. Second, a laser (or an LED) with a wavelength below 375 nm removes one of the valence electrons by exciting it to the continuum, thus resulting in singly ionized Calcium.
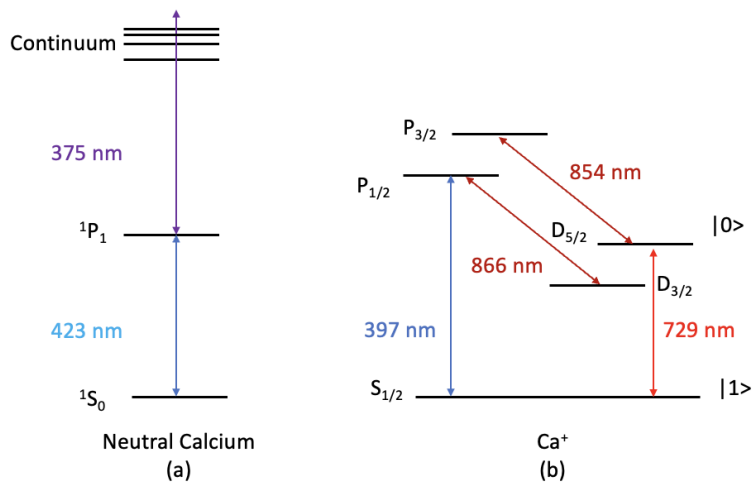


Figure 2: Atomic structure of Calcium. The neutral Calcium atom (a) undergoes two-step photo-ionization; the resulting $^{40}Ca^+$ ion (b) can undergo various transitions for qubit manipulation.

The $^{40}Ca^+$ ion can undergo dipole transitions at 397 nm, 854 nm and 866 nm. The transition at 397 nm has a large linewidth of 22.4 MHz and a short lifetime of about 7 ns, making it good for scattering photons [12]. The transitions at 854 nm and 866 nm are used for repumping. All of these transitions are driven incoherently in our experiments, so the phase of the light is not crucial.

Besides dipole transitions, $^{40}Ca^+$ can undergo a quadruple transition from

the $S_{1/2}$ state to the $D_{5/2}$ state by a laser at 729 nm. The transition has a natural linewidth of only 136 mHz, corresponding to a long lifetime of approximately 1 s [3]. Since this feature allows for stable and coherent operations, we use the transition for qubit manipulation. In this case, precise control over the laser's frequency and phase becomes crucial.

## 1.2 Requirements for laser frequency control

Table 1 shows the requirements for the different lasers' frequency control. For the dipole transitions, the linewidth of the lasers out of the box is narrow enough. Therefore we only need to fight against the slow drifts. For the quadruple transition at 729 nm, however, we need to both narrow down the linewidth and counteract the slow drifts.

| Wavelength | Usage | Required frequency accuracy | Required linewidth |
|---|---|---|---|
| 375 nm | Photo-ionization | None | None |
| 423 nm | Isotope selective photo-ionization | 10 MHz | 10 MHz |
| 397 nm | Cooling, preparation, detection | 1 MHz | 1 MHz |
| 854 nm | Repumping | 10 MHz | 1 MHz |
| 866 nm | Repumping | 10 MHz | 1 MHz |
| 729 nm | Qubit manipulation | 1 Hz | 1 Hz |

Table 1: Frequency control requirements for different lasers.

### 1.2.1 Counteracting slow laser frequency drifts

For the lasers driving dipole transitions, the linewidth of commercially available external-cavity diode lasers (ECDLs) is already sufficiently narrow. They do however exhibit drifts on slow timescales that have to be eliminated.

One of the primary reasons for laser frequency drifts on long timescales are air pressure fluctuations, as illustrated in Figure 3. Opening or closing the door between the control room and the preparation area in our laboratory causes a pressure change of about 0.5 mbar which leads to a frequency shift of 40 MHz. Similarly, due to air pressure changes throughout the day, the 729 nm lasers can drift over 100 MHz as shown in Figure 4, with an increase in pressure causing a decrease in laser frequency.

These slow frequency drifts can be eliminated by stabilizing the laser frequency to a more reliable frequency reference through a feedback loop, where a loop bandwidth of about 1 kHz is enough.
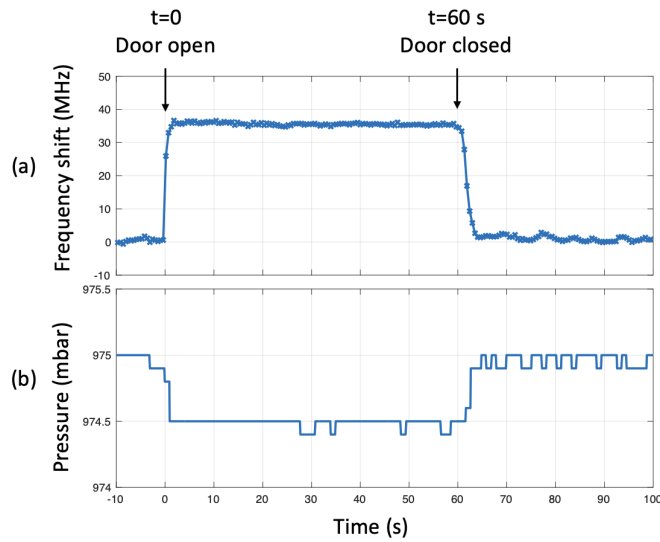
Figure 3: Frequency shift of a 729 nm diode laser by opening and closing the lab door. The frequency changed about 40 MHz (a) due to a pressure change of about 0.5 mBar (b).
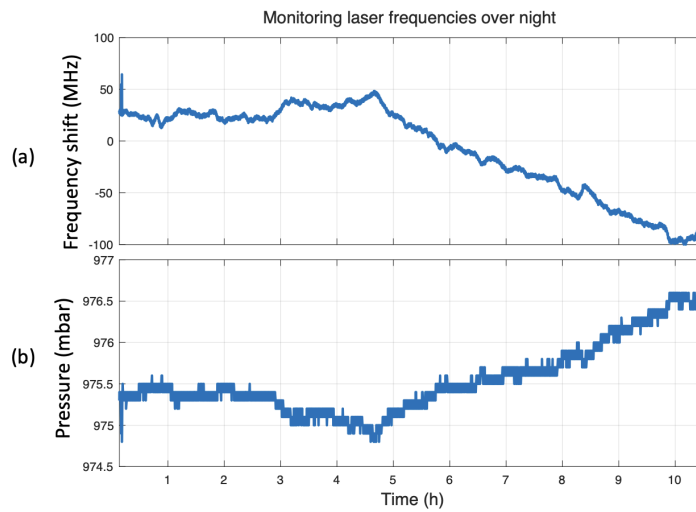


Figure 4: Frequency shift of a 729 nm diode laser overnight. The laser drifted over 100 MHz (a) due to a pressure change of more than 1.5 mBar (b).

### 1.2.2 Counteracting fast frequency drifts

In order to drive the 729 nm transition in $^{40}\text{Ca}^+$, we want a laser with a linewidth of about a Hertz. As the linewidth of commercial lasers is typically much larger than that, we need to perform linewidth-narrowing. We can do so by making the feedback loop stabilizing the laser frequency fast such that it not only counteracts the slow but also the fast frequency drifts of the laser.

The process of linewidth narrowing is conceptually illustrated in Figure 5, which shows the frequency noise power spectral density (PSD) of the laser when free-running (dashed line) and when locked (solid line). By using the feedback loop, the PSD of the free-running laser is reduced at frequencies below $\omega_{\text{srv}}$, leading to linewidth-narrowing. This is captured by the $\beta$-separation line [8]: Noise above it contributes to the linewidth of the narrow central peak, whereas noise below it only contributes to the wings around the narrow central peak in the optical spectrum of the laser.

In order to implement single-qubit gates, having a narrow laser linewidth is only a necessary but not sufficient criterion, as discussed in [7]. There they introduced the $\chi$-separation line that is also shown in Figure 5. Again, noise above the $\chi$-separation line contributes to excess gate infidelity, whereas noise below it does not. As illustrated, the $\chi$-separation line typically places more stringent requirements on the laser frequency PSD than does the $\beta$-separation line. Furthermore, the $\chi$-separation depends on the gate speed and becomes ever more stringent as the gate speed is increased. An intuitive explanation for this is that high-frequency laser noise can not be averaged away if the gate time becomes ever shorter.
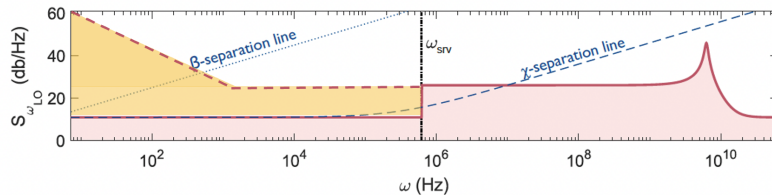


Figure 5: Conceptual illustration of the frequency noise PSD of a diode laser, adapted from [7]. The frequency noise of the locked laser (solid red line) is obtained by virtue of a feedback loop reducing the frequency noise of the free-running laser (dashed red line), here up to the frequency $\omega_{\text{srv}}$. Noise above the $\beta$-separation line contributes to the laser linewidth, and noise above the $\chi$-separation line contributes excess infidelity to single-qubit gates. Typically, the $\chi$-separation line puts much more stringent requirements on the laser frequency noise PSD than the $\beta$-separation line alone, as shown here.

In order to implement two-qubit gates, we also want the laser to have a clean optical spectrum around the narrow central peak. The reason for this is that

two-qubit gates are typically implemented by driving the motional sideband transitions of the trapped ions. To do so, we tune the frequency of the laser such that it coincides with the sideband to be driven, as illustrated in Figure 6(b). However, when doing so, the carrier can be driven off-resonantly by the side lobes of the optical spectrum of the laser. This is exacerbated by the carrier transition typically being much stronger than the sideband transitions and is one of the leading errors in entangling gate operations [16]. Accordingly, we want the side lobes to be well below the narrow central carrier.
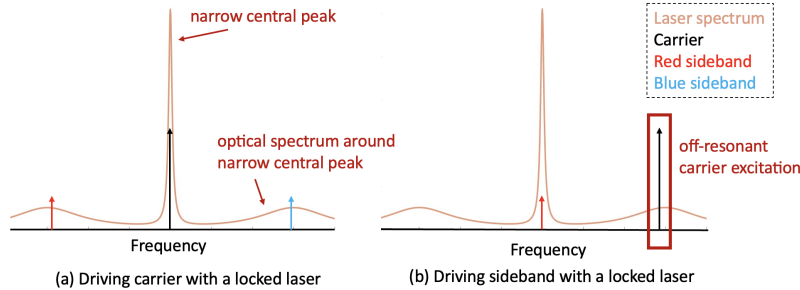


Figure 6: The importance of the optical spectrum of the laser. (a) When driving a carrier transition, the effect of the side lobes in the spectrum of the lasers is suppressed, as the carrier transition is much stronger than the sidebands. (b) When driving a sideband transition (here the red sideband), the situation is reversed, and the carrier can easily get driven off-resonantly, leading to errors.

## 1.3   Typical lasers

For the dipole transitions, we use external cavity diode lasers (ECDLs) for convenience. For the 729 nm lasers, we use an ECDL or a Ti:Sapphire laser for performance. As shown in Figure 7, the Ti:Sa laser (red) has a cleaner noise PSD than ECDL (blue). Therefore, in order to implement single and two-qubit gates with high fidelity, the Ti:Sa laser is particularly favorable for our experiment.
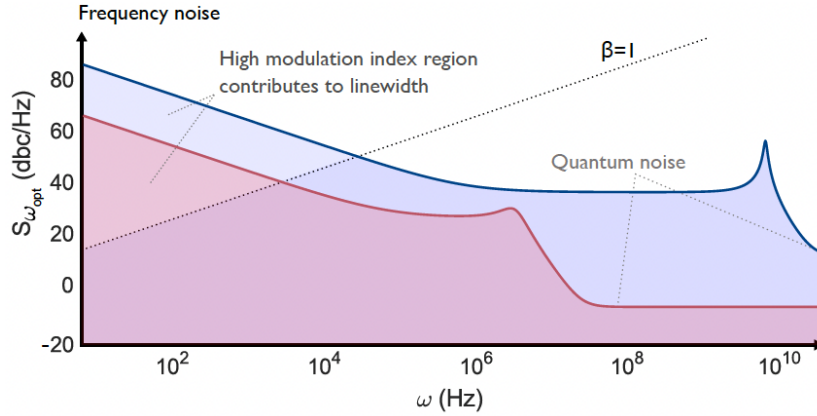
Figure 7: Schematic free-running laser frequency noise PSDs, adapted from [7]. Blue: diode laser; red: solid-state laser. The $\beta = 1$ line separates the noise that contributes to the laser linewidth and the noise that contributes to the wings of the laser lineshape. The solid-state laser has significantly lower noise compared to the diode laser, especially at high frequencies.

### 1.3.1 Diode laser

Laser diodes generate an optical gain by applying a voltage across a p–n junction. When a forward bias voltage is applied, electrons and holes are injected into the depletion region of the junction. Within this region, electron-hole recombination occurs, resulting in the emission of photons. The emitted photons undergo further amplification through the process of stimulated emission.

Diode lasers are compact, efficient, and cheap, but usually have a large laser linewidth. An external cavity can narrow down a free-running linewidth to $10\,\mathrm{kHz}$ [22], as illustrated in Figure 8. The external cavity usually consists of a resonator with a mirror on one end and a grating on the other end. The zeroth-order beam is the laser output, while the first-order beam is reflected back for feedback. The wavelength can be tuned by adjusting the grating angle.

9
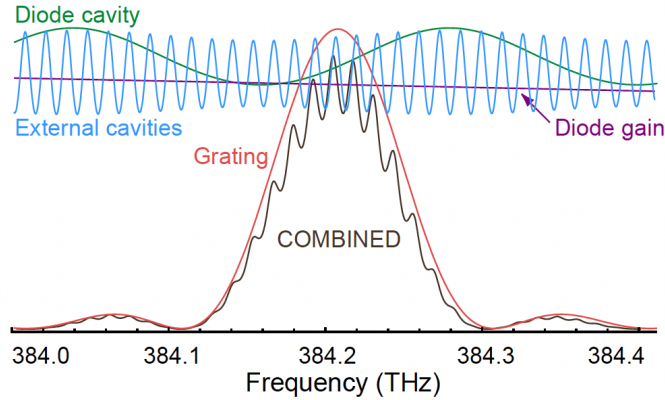
Figure 8: Schematics of the frequency determination of an ECDL, adapted from [15]. The external cavity (blue) provides a narrower linewidth of the laser output, and the grating (red) allows for wavelength tuning.

Our group uses two Modular Amplified Tunable Single-Mode Lasers (MTA pro) from TOPTICA. The configuration is illustrated in Figure 9. It comprises an ECDL connected to a tapered amplifier (TA pro or BoosTA pro). The TA can amplify the laser power to several Watts while maintaining a good beam quality [20]. The laser driving electronics is the digital laser controller (DLC pro), which allows for convenient remote operation. A fast lock can be achieved by combining the DLC pro Lock with the Fast Analog Linewidth Control (FALC pro).
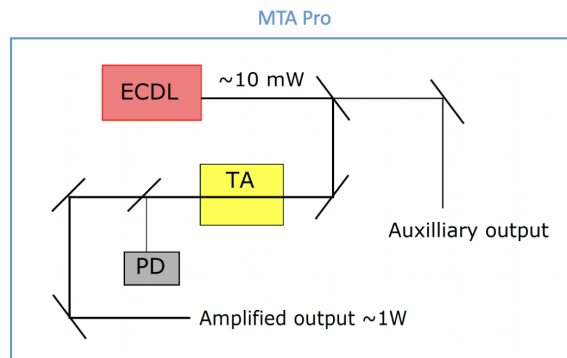


Figure 9: Layout of a TOPTICA MTA pro system. It is a module with ECDLs connected to tapered amplifiers (TA). Automatic beam alignment of the light going into the TA can be achieved with a photodiode (PD).

### 1.3.2   Ti:Sapphire laser

In addition to the ECDLs, we also use one Ti:Sa laser from MSquared. A small amount of $Al^{3+}$ is substituted with $Ti^{3+}$ in an $Al_2O_3$ crystal in a melt process, where $Ti^{3+}$ ions are responsible for lasing [14]. Ti:Sa has a broad absorption spectrum from approximately 400 nm to 600 nm, and we use a diode pump laser at 532 nm. The Ti:Sa laser also has a broad emission spectrum from 670 nm to above 1000 nm[1].

The Ti:Sa laser has a unique cavity geometry to achieve a narrow linewidth as shown in Figure 10. The ring resonator avoids standing-wave formation inside the cavity. With this feature, the gain is not saturated, so the spatial hole burning in the laser crystal is reduced. This results in better single-frequency operation and a narrower linewidth.

The wavelength can be roughly tuned by the motorized intracavity birefringent filter (BRF), which introduces a wavelength-dependent loss into the cavity [14]. Fine-tuning of the wavelength is achieved by adjusting the spacing of the intra-cavity etalon. With a modulation frequency of 19.4 kHz, the transmission peak of the etalon is synchronized with the transmission peak of the laser cavity mode, resulting in a narrower linewidth.
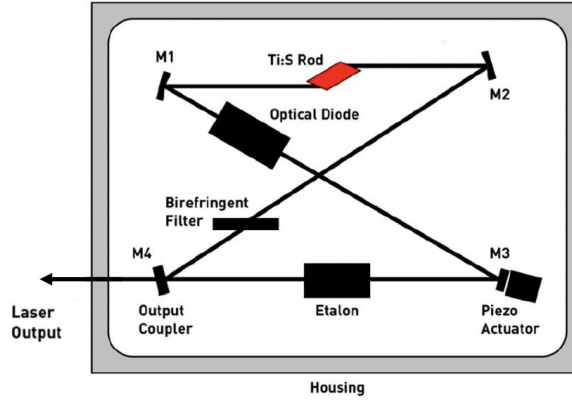


Figure 10: Illustration of the SolsTiS laser cavity design [14]. Our model additionally features an intra-cavity EOM for fast frequency control (not shown).

---

[1]The pump laser from MSquared is called Equinox and the Ti:Sa laser is called SolsTiS.

# 2 Introduction to Feedback Control

To transfer the good stability of a reference to the laser, a feedback loop is used to continuously measure the laser's frequency and correct the errors.

## 2.1 Basic loop shape

A basic feedback loop consists of a sensing part $(H)$, a controller $(C)$, an actuator $(P)$, and a time delay $(TD)$, as shown in Figure 11. Each block results in a frequency-dependent gain and phase shift to an input signal.

The laser frequency $y$ fluctuates due to the disturbance $d$. The frequency is compared with a stable reference $r$, where the error $e$ is sent to the controller. The controller then sends a signal $u$ to the actuator to correct the frequency. These time-domain signals can also be represented in the frequency domain by capital letters.
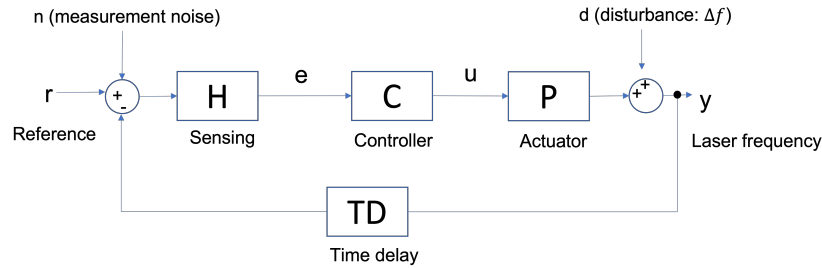


Figure 11: Illustration of a basics feedback loop. The laser's frequency $y$ is compared with the reference $r$. The error $e$ is sent to the controller, which outputs a signal $u$ to the actuator to counteract the disturbance.

The **loop gain** is defined as the product of the gains of all the components in the loop:

$$L(s) = H(s)C(s)P(s)TD(s). \tag{1}$$

where $s = j\omega$.

The **disturbance attenuation**, or sensitivity function, captures how well the disturbances D are suppressed on the laser frequency Y

$$S(s) \equiv \frac{Y(s)}{D(s)} = \frac{1}{1 + L(s)}. \tag{2}$$

$|S| \ll 1$ means the system suppresses noise effectively, $|S| = 1$ implies the loop does nothing, and $|S| > 1$ means the disturbance is amplified.

Correspondingly, the **reference following**, or the complementary sensitivity function, is defined as

$$T(s) \equiv \frac{Y(s)}{R(s)} = \frac{L(s)}{1 + L(s)} = \frac{Y(s)}{N(s)}. \tag{3}$$

It describes how well the laser frequency Y tracks the reference R. However, as the feedback loop has no way of telling apart the reference R from the measurement noise N, T also captures how well measurement noise is imprinted onto Y. Together, we can see that $T(s) + S(s) = 1$.

A typical loop gain $L(s)$ should be approximately inversely proportional to the frequency. The behavior of $T(s)$ and $S(s)$ based on this $L(s)$ is depicted in Figure 12. When $|L(s)| \gg 1$, the feedback loop is active. It effectively tracks the reference ($|T(s)| \approx 1$) and attenuates disturbance ($|S(s)| \ll 1$). When $|L(s)| \ll 1$, the low gain shows that the feedback loop is turned off. The loop no longer suppresses disturbance ($S(s) \approx 1$) and no longer tracks the reference ($T(s) \approx 0$), which is beneficial, as that also means that it will not imprint high-frequency measurement noise. The transition between these two regimes happens around the gain crossover frequency $\omega_{gc}$, where the loop gain has unity magnitude, i.e. $|L(s)| = 1$. Accordingly, the gain crossover frequency is a useful measure for the bandwidth of the feedback loop.
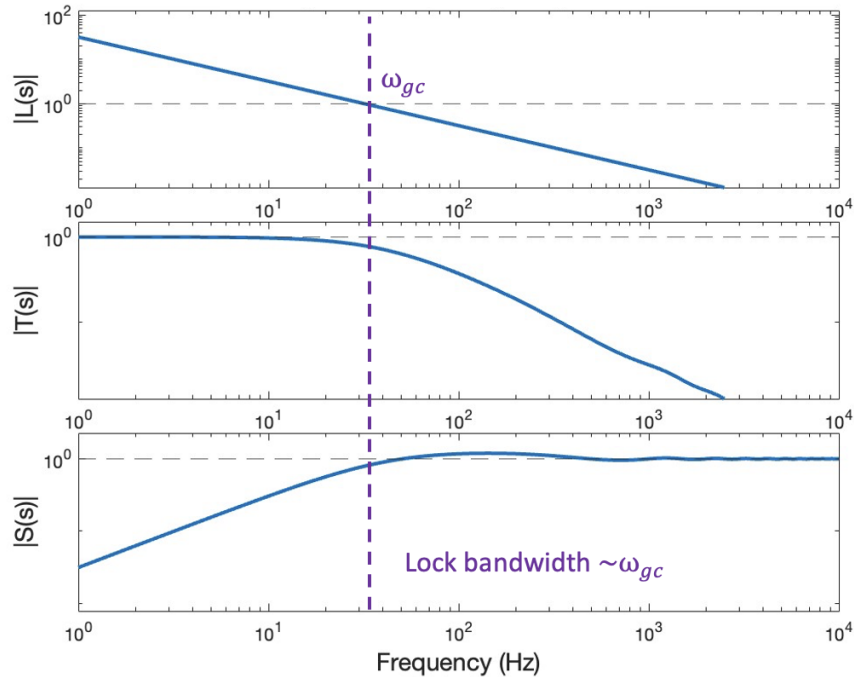


Figure 12: Typical behavior of L, S and T in a basic feedback loop with only time delay $L(s) = \frac{g}{s} \cdot \exp(-sT)$. The bandwidth of the feedback loop can be approximated by the gain crossover frequency $\omega_{gc}$.

When the loop gain is increased, as shown in Figure 13, the lock bandwidth increases so the feedback performance improves. However, if the gain is too

high, $T(s)$ and $S(s)$ show peaking just above $\omega_{gc}$ (servo bump), indicating that the loop has poor stability and robustness. Therefore, the frequency of the servo bump is a coarse estimation of the loop bandwidth.
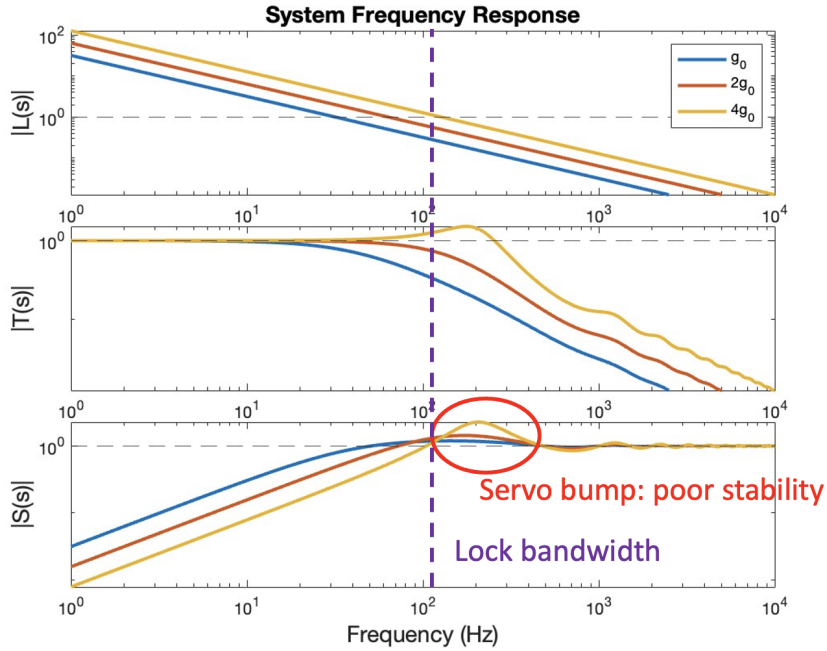


Figure 13: Frequency response of the same feedback loop $L(s) = \frac{g}{s} \cdot \exp\left(-sT\right)$ with different gains $g$. Increasing the loop gain improves the feedback loop performance and lock bandwidth, but excessive gain may lead to loop instability. The lock bandwidth can be estimated as the frequency of the servo bump.

## 2.2 Stability of the feedback loop

From Eq.(2) and (3), we can see that instability starts when $L(s) = -1$. At this point, the system acts so fast that it is $180°$ out of phase with the reference, resulting in oscillatory behaviors [4]. As a result, the stability of a feedback loop requires $L(s)$ to stay away from the instability point $-1$.

As shown in Figure 14, the **phase margin** indicates the amount of phase delay that can be tolerated before instability occurs [4]. At the frequency $\omega_{gc}$, the phase margin is the additional phase shift required to reach $-180°$. As the loop gain increases, the phase margin decreases. Eventually, a poor phase margin leads to strong peaking in $S(s)$ like in Figure 13.

Similarly, the factor to increase the gain to 1 before reaching the $-180°$ phase delay is the **gain margin**. It shows the gain we can increase until instability

begins. To have good stability, we usually want the gain margin $\geq 2$ and phase margin $\geq 60°$ [4].
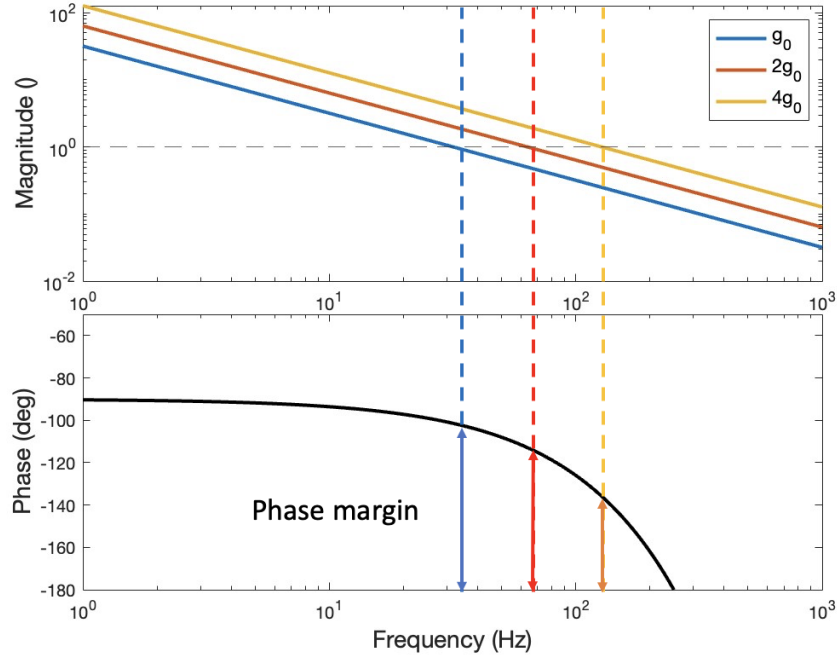


Figure 14: Behavior of a basic $L(s)$ at different gains. The phase margin indicates the amount of phase delay that can be tolerated before instability begins. Increasing the gain crossover will reduce the phase margin.

Time delay in feedback loop leads to rapid phase drop. At high frequencies, it is often the limiting factor for the loop bandwidth. In general, a time delay of T limits the achievable gain crossover frequency to

$$f_{\text{gc}} \leq \frac{1}{10 \cdot T}. \tag{4}$$

This is because a delay of T results in $360°$ of phase lag at a frequency $\frac{1}{T}$. Since the integrator loop gain $1/s$ already takes $90°$ phase lag, we can at most tolerate another $90°$. For convenience, suppose we get $36°$ phase lag from the time delay, then this gives a loop bandwidth of $\frac{1}{10 \cdot T}$.

Table 2 shows the time delay of different controllers and the resulting bandwidth limits due to them:

| Controller | Time Delay | Achievable $f_{\mathrm{gc}}$ |
|---|---|---|
| DLC pro | $10\,\mu\mathrm{s}$ | $10\,\mathrm{kHz}$ |
| Fast digital controller | $100\,\mathrm{ns}$ | $1\,\mathrm{MHz}$ |
| FALC Pro | $10\,\mathrm{ns}$ | $10\,\mathrm{MHz}$ |

Table 2: Time delay and the corresponding achievable gain crossover frequency for different controllers. Analog controllers have a much shorter time delay than digital controllers, allowing for a larger gain crossover frequency.

## 2.3 PI/PID Controller

In the time domain, the output of a PID controller with an input error signal $e(t)$ is

$$u_{\mathrm{PID}}(t) = K_P \cdot e(t) + K_I \int e(t)dt + K_D \frac{de(t)}{dt}. \tag{5}$$

In the frequency domain, the response of the controller is

$$
\begin{aligned}
C_{\mathrm{PID}}(s) &= k \cdot C_{\mathrm{PI}} \cdot C_{\mathrm{D}} \\
&= k(1 + \frac{\omega_I}{s})(1 + \frac{s}{\omega_D})
\end{aligned} \tag{6}
$$

where $k$ is the overall gain, $\omega_I$ is PI corner frequency, and $\omega_D$ is the D corner frequency (Figure 15). This shows how the controller can amplify or attenuate signals at arbitrary frequencies.
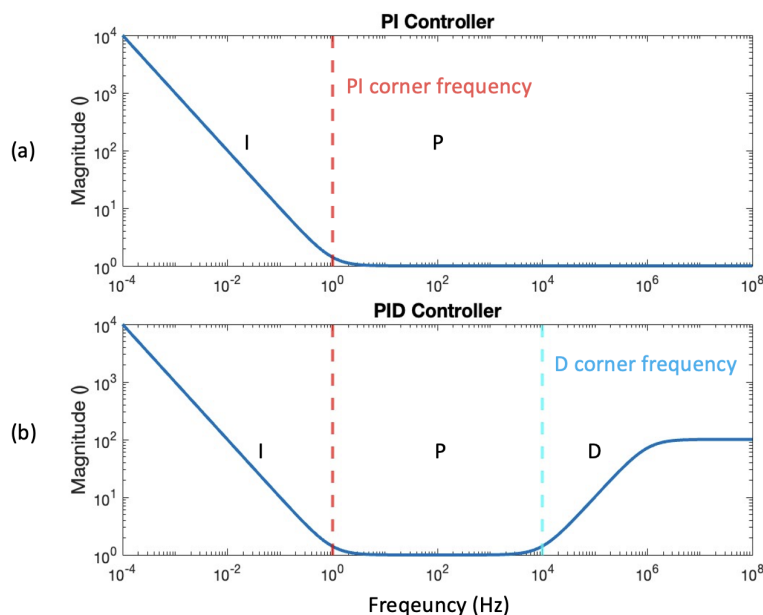


Figure 15: Frequency responses of the PI and PID controllers.

Starting with the desired basic loop gain $L_{\text{des}}(s) = \omega_{gc}/s$, we can design the controller $C(s)$ based on the shape of the sensor $H(s)$ and actuator $P(s)$:

$$C_{\text{des}}(s) = \frac{L_{\text{des}}(s)}{H(s)P(s)} \tag{7}$$

The controller selection process is depicted in Figure 16. A fast controller or actuator has a flat frequency response; while a slow one behaves like a low-pass filter: it is flat at low frequencies but rolls off at higher frequencies. In the case of a fast detector and fast controller, we should use an integral-only controller. For a fast controller with a slow actuator, or a slow controller with a fast actuator, a PI controller would be an appropriate choice. Finally, if both the controller and the actuator are slow, a PID controller is needed. However, in this case, changing to a faster sensor or actuator is often the better choice.
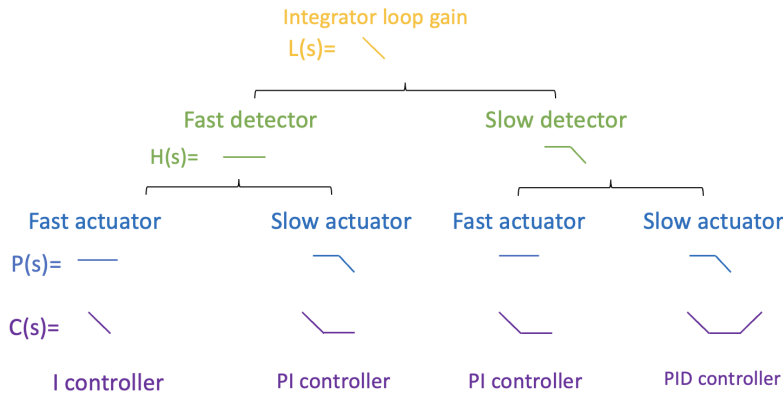


Figure 16: Selection of controller $C(s)$ in different situations. Fast detector and actuator only require an integrator controller; only one of them is fast requires a PI controller; slow detector and actuator requires a PID controller.

## 2.4 Closed-loop characterization

To characterize a feedback loop, we can inject a sinusoidal probe signal at different frequencies through a summing junction. We then measure the responses at different points of the loop, as illustrated in Figure 17. Coherent averaging is used to recover the response that is in phase with our injected signal while averaging away the laser's random noise.
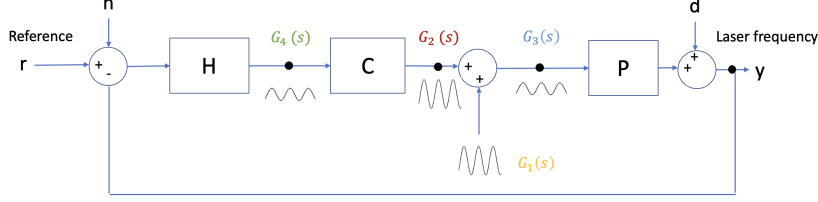
Figure 17: Diagram for characterizing a feedback loop. A sinusoidal probe signal is injected through a summing junction and the responses at different points are measured.

The disturbance attenuation $S(s)$ is the signal right after the summing junction with respect to the probe signal

$$S(s) = \frac{G_3(s)}{G_1(s)}, \tag{8}$$

while the reference following $T(s)$ is measured before the summing junction

$$T_{\mathrm{raw}}(s) = \frac{G_2(s)}{G_1(s)}. \tag{9}$$

If there is any attenuator or amplifier before the measuring point, the frequency response should be re-normalized with an open-loop measurement $S_{\mathrm{open}}(s)$ by breaking the loop. For example, a re-normalization of $S(s)$ is done by

$$S(s) = \frac{S_{\mathrm{raw}}(s)}{S_{\mathrm{open}}(s)}. \tag{10}$$

With $S(s)$ and $T(s)$, the loop gain can be obtained

$$L(s) = \frac{T(s)}{S(s)} = \frac{G_2(s)}{G_3(s)}. \tag{11}$$

Eq.(11) can also be understood by considering the signal going around the loop, accumulating a loop gain of $L(s)$.

Furthermore, the signal before and after the controller can be used to characterize the controller

$$C(s) = \frac{G_2(s)}{G_4(s)}. \tag{12}$$

After obtaining all of the above, we can also calculate the combined frequency response of the remaining part of the loop

$$H(s)P(s)TD(s) = \frac{L(s)}{C(s)}. \tag{13}$$

For more details see [17, Chapter 3.6].

18

# 3    Laser Frequency Stabilization

After introducing the basics of a feedback loop, we now look specifically at our frequency stabilization system. We chose an optical cavity as the stable reference to compare the laser's frequency.

## 3.1    Properties of optical cavities

The transmission spectrum of an optical cavity is illustrated in Figure 18. The free spectral range (FSR) of a cavity is the frequency spacing of the axial modes of an optical resonator [19]. In the case of a fabry-perot cavity, it is

$$\text{FSR} = \frac{c}{2L}, \tag{14}$$

where $L = 10\,\text{cm}$ is the length of the cavity, resulting in a FSR of $1.5\,\text{GHz}$.

The finesse of an optical cavity is a measurement of how narrow its resonance modes are [18]. A higher finesse indicates a sharper resonance (a narrower cavity linewidth). The finesse is defined by the FSR divided by the cavity linewidth (FWHM), and is completely determined by the cavity mirrors' reflectivities $R_1$ and $R_2$ [9]:

$$\mathcal{F} \equiv \frac{\text{FSR}}{\text{FWHM}} = \frac{\pi(R_1 R_2)^{1/4}}{1 - \sqrt{R_1 R_2}}. \tag{15}$$
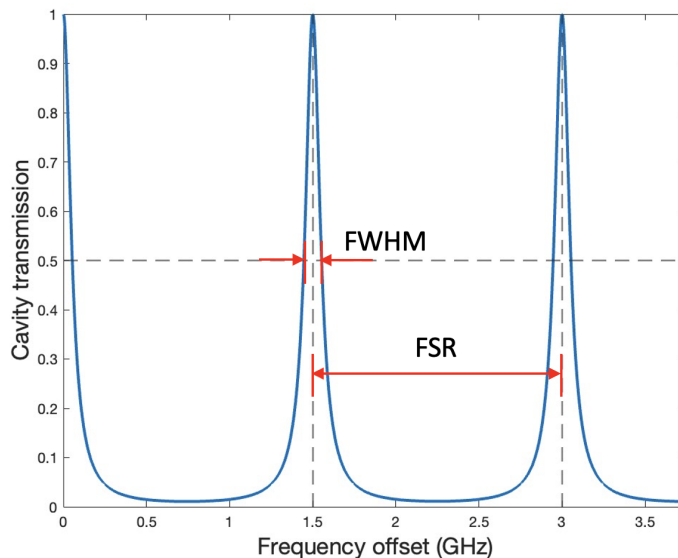


Figure 18: Cavity transmission spectrum with a free-spectral range of $1.5\,\text{GHz}$, FWHM $= 0.1\,\text{GHz}$, giving a finesse of 15.

The finesse not only measures the sharpness of the cavity mode but also measures how well the light is stored in the cavity. Suppose a planar cavity has mirrors with both reflectivities equal to $R$. At the time $t = 0$, there are $N$ photons inside the cavity. After traveling half of the cavity at $t = \frac{nL}{c}$, where $n$ is the refractive index, the remaining photon number is $RN$. We can write it as

$$\frac{dN}{dt} = \frac{\Delta N}{\Delta t} = -\frac{(1-R)N}{nL/c} = -\frac{c(1-R)N}{nL}, \tag{16}$$

and the solution is

$$N(t) \quad = \quad N_0 e^{-t/\tau} \tag{17}$$

where we define the photon lifetime inside the cavity as

$$\tau = \frac{nL}{c(1-R)}. \tag{18}$$

The spectral FWHM in Hz is related to finesse by the relation [9]

$$\text{FWHM} = \frac{c}{2n\mathcal{F}L}, \tag{19}$$

For $R \to 1$, Eq.(15) becomes $\mathcal{F} \approx \frac{\pi}{1-R}$. Plugging this expression into Eq.(19), we get

$$\text{FWHM} = \frac{c\pi}{2nL(1-R)} = \frac{1}{2\pi\tau}. \tag{20}$$

Therefore, the finesse also measures the photon storage time inside the cavity

$$\mathcal{F} = \frac{\text{FSR}}{\text{FWHM}} = \text{FSR} \cdot 2\pi\tau, \tag{21}$$

This provides a convenient way to measure the finesse. When the laser is locked, the light inside the cavity is in a steady state, and the transmitted light is at maximum power. Suddenly unlocking or turning off the laser, the intensity of the transmitted beam will exponentially decay as in Eq.(17):

$$y(t) = A + Be^{-t/\tau}, \tag{22}$$

where $y$ is the photodiode voltage, A is the DC offset from the ambient light and B is the transmitted light. This is called the cavity **ring-down measurement**. By fitting the measured data with the exponential curve, one can easily extract $\tau$ and obtain the finesse via Eq.(21).

As an example, the plot for ring-down measurement of high-finesse cavity C is shown in Figure 19. The photodiode used for such measurements should have a bandwidth well above the cavity linewidth such that we only record the transient due to the light in the cavity decaying and not the transient of the photodiode.
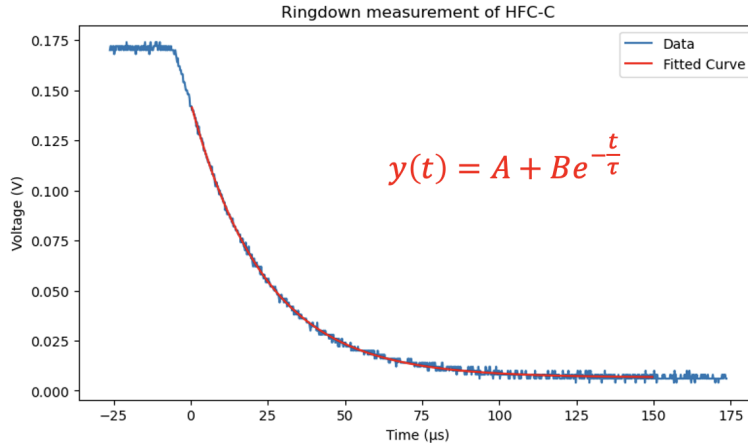
Figure 19: Ring-down measurement of high-finesse cavity C, fitted with an exponential decay curve. The decay time $\tau$ is about $24\,\mu s$.

Table 3 shows the results for all three high-finesse cavities in our lab.

| Cavity name | A | B | C |
|---|---|---|---|
| Decay time | $26.34\,\mu s$ | $22.03\,\mu s$ | $23.80\,\mu s$ |
| Cavity FWHM | $6042\,Hz$ | $7223\,Hz$ | $6688\,Hz$ |
| Finesse | $248\,240$ | $207\,659$ | $224\,266$ |

Table 3: Results of ringdown measurements of all three high-finesse cavities in our lab.

## 3.2    PDH error signal generation technique

The top-of-fringe Pound-Drever-Hall (PDH) locking technique uses the reflected light from the cavity to generate an error signal for the feedback loop. The PDH implementation is illustrated in Figure 20. An introduction to the PDH technique can be found at [5].
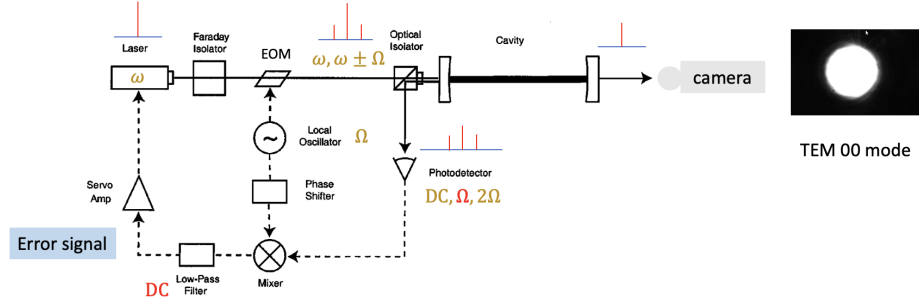
Figure 20: PDH lock implementation, adapted from [5]. The carrier with frequency $\omega$ is phase-modulated by an EOM and sent to the cavity. The reflected beams interfere with each other on the photodiode. The field oscillating at $\Omega$ carries the information of the error signal. This field is demodulated with a mixer to become a DC signal.

The incident beam $E_{\text{inc}}(t)$ at carrier frequency $\omega$ is phase-modulated by an electro-optic modulator (EOM)

$$E_{\text{inc}}(t) = E_0 e^{i(wt+\beta \sin \Omega t)}, \tag{23}$$

where $\beta$ is the modulation depth and $\Omega$ is the modulation frequency. When $\beta$ is small, this expression can be approximated as

$$E_{\text{inc}}(t) \approx E_0[J_0(\beta)e^{i\omega t} + J_1(\beta)e^{i(\omega+\Omega)t} - J_1(\beta)e^{i(\omega-\Omega)t}], \tag{24}$$

where $J_n(\beta)$ is the $n$-th Bessel function.

The reflected beam's field can be treated as separate beams interfering with each other, where we multiply each beam's reflection coefficient

$$F(\omega) = E_{\text{ref}}/E_{\text{inc}} = \frac{r \cdot \exp(i\frac{\omega}{\text{FSR}} - 1)}{1 - r^2 \exp(i\frac{\omega}{\text{FSR}})}. \tag{25}$$

In the PDH setup, the reflected beams come from the sidebands and the carrier. The sidebands are fully reflected $F(\Omega) \approx \pm 1$. A part of the carrier is also reflected, consisting of the promptly reflected beam, which never enters the cavity; and the leakage beam, which is the standing wave inside the cavity that leaks back through the first mirror.

The resulting power of the reflected beam $P_{\text{ref}} = |E_{\text{ref}}|^2$ consists of terms oscillating at DC, $\Omega$, and $2\Omega$ frequencies. Among them, the sideband signal interfering with the carrier signal (the part with $\Omega$) carries the information of the error signal (the reflected beam's phase). This error signal $\epsilon$ can be separated by mixing the RF signal with a sinusoidal signal at $\Omega$ and then going through a low-pass filter

22

$$\epsilon \propto \text{Im}[F(\omega)F^*(\omega + \Omega) - F^*(\omega)F(\omega + \Omega)]. \qquad (26)$$

The error signal in Eq.(26) is plotted in Figure 21. The capture range is $\pm\Omega$ (colored in light yellow). In the middle, the slope is very steep and approximately linear (green) for $\pm$HWHM/3.
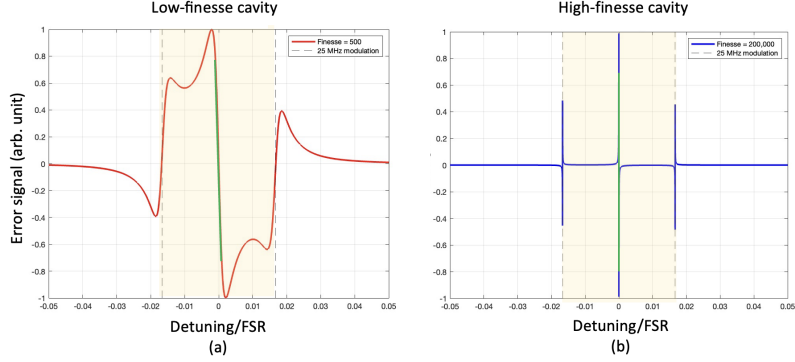


Figure 21: PDH error signals with fast modulation for low-finesse cavity with $\mathcal{F} = 500$ (a) and high-finesse cavity with $\mathcal{F} = 200,000$ (b). The capture ranges (light yellow) are both $\pm\Omega = 25\,\text{MHz}$. The slope in the middle is steeper for the high-finesse cavity.

However, there is often a phase mismatch between the PDH RF input signal and the local oscillator signal. The error signal is reduced at the center and becomes asymmetric at the sidebands as shown in Figure 22. By optimizing the phase, the amplitude of the PDH error signal can be maximized, which results in a larger loop gain. In practice, we have found it convenient to adjust the phase while measuring $S(s)$, as the best phase minimizes $S(s)$.
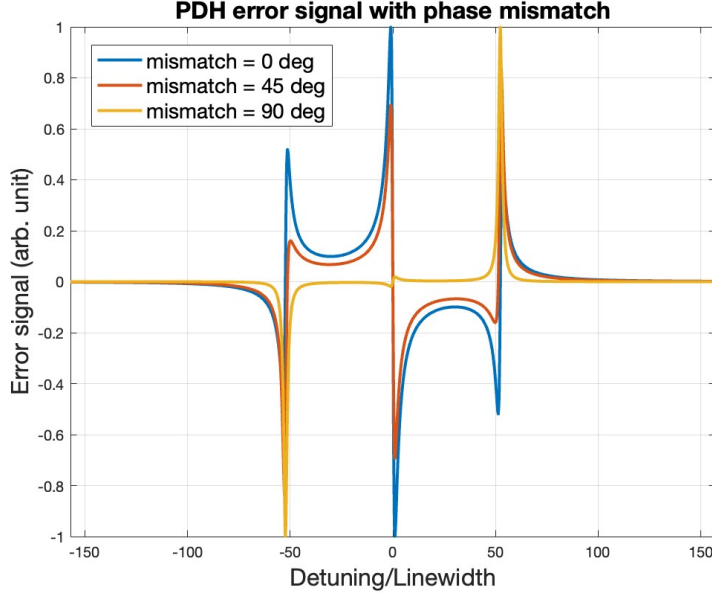
Figure 22: PDH error signal (in the fast modulation regime) demodulated with a mixer at different phase mismatches: 0, 45, and 90 degrees. With the phase mismatch, the error signal is smaller at the resonance and asymmetric at the sidebands.

Additionally, the slope of the PDH error signal can be optimized by finding the best EOM driving power. The power of the carrier is $P_C = J_0^2(\beta)P_0$ and the power in each first-order sideband is $P_S = J_1^2(\beta)P_0$, where $\beta$ is the modulation depth and $P_0$ is the total power in the incident beam. The slope of the PDH error signal is proportional to the intensity of the carrier interfering with the first-order sideband

$$\epsilon \propto \sqrt{P_C P_S} \propto J_0(\beta)J_1(\beta) \tag{27}$$

as plotted in Figure 23.

Since $\beta$ is linearly proportional to the RF-signal amplitude [10], we can tune $\beta$ to maximize the error signal. In practice, we again found it convenient to adjust the RF power while minimizing $S(s)$.
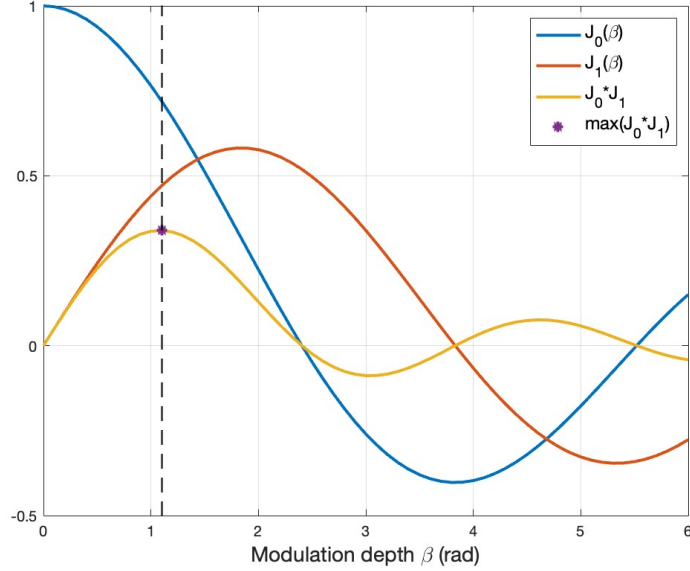
Figure 23: Carrier (blue) and sidebands (red) signal intensities based on the bessel functions. The error signal (yellow) is proportional to the carrier interfering with the sidebands. The optimal error signal happens where the modulation depth is around 1.1 rad.

## 3.3 Dynamics of PDH

The PDH error signal is generated by collecting the reflected light from the cavity. As mentioned before, this reflected light consists of two components: the promptly reflected beam, which does not enter the cavity at all, and the leakage beam, which is the standing wave inside the cavity that leaks through the front mirror.

In the case of a step change in the laser frequency, as shown in Figure 24a), the cavity requires some time to transit from the old light to the new light, as illustrated in Figure 24b). The original photons in the cavity exhibit an exponential decay as they gradually leave the cavity, just like in the ring-down measurement. Meanwhile, the new photons take an exponential growth time until they reach a steady state $y(t) = 1 - e^{-t/\tau}$, where $y$ is the field inside the cavity and $\tau = \frac{1}{\omega_{\text{HWHM}}}$ is the storage time constant.
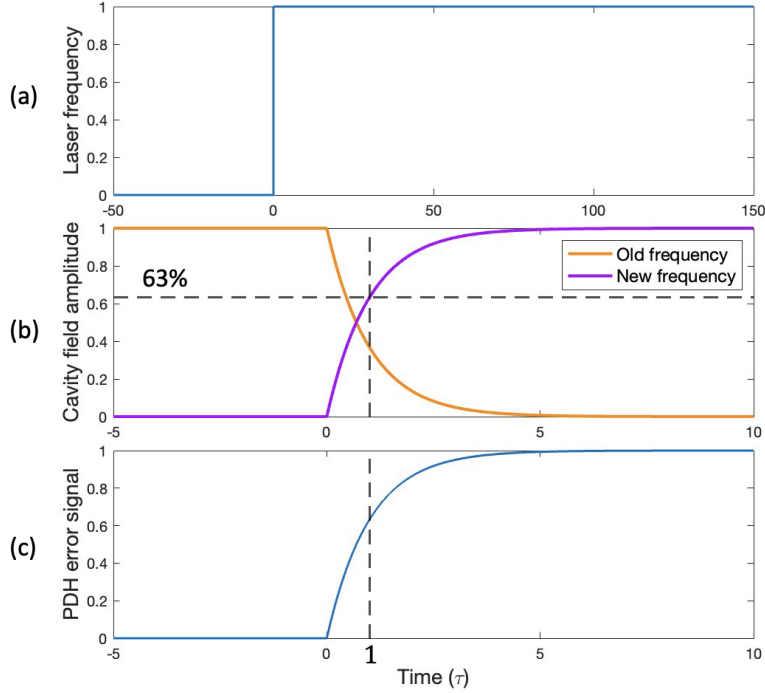
Figure 24: A step change of the laser frequency (a) causes the cavity to respond by emptying out the old frequency light and filling up with the new frequency light in an exponential time (b). The process also shows the step response of the PDH technique to be exponential (c).

In the frequency domain, this PDH error signal response corresponds to a first-order low-pass filter

$$H_{\mathrm{PDH}}(s) \propto \frac{\mathcal{F}}{1 + s/\omega_{\mathrm{HWHM}}}. \tag{28}$$

The response of the PDH technique is flat at low frequency, which detects the frequency difference between the incoming laser beam and the field inside the cavity. At high frequencies, the PDH technique behaves like an integrator, measuring the phase difference between the incoming beam and the cavity field. Figure 25 shows the frequency response of a low-finesse cavity with a HWHM of $1\,\mathrm{MHz}$ and a high-finesse cavity with a HWHM of $1\,\mathrm{kHz}$.
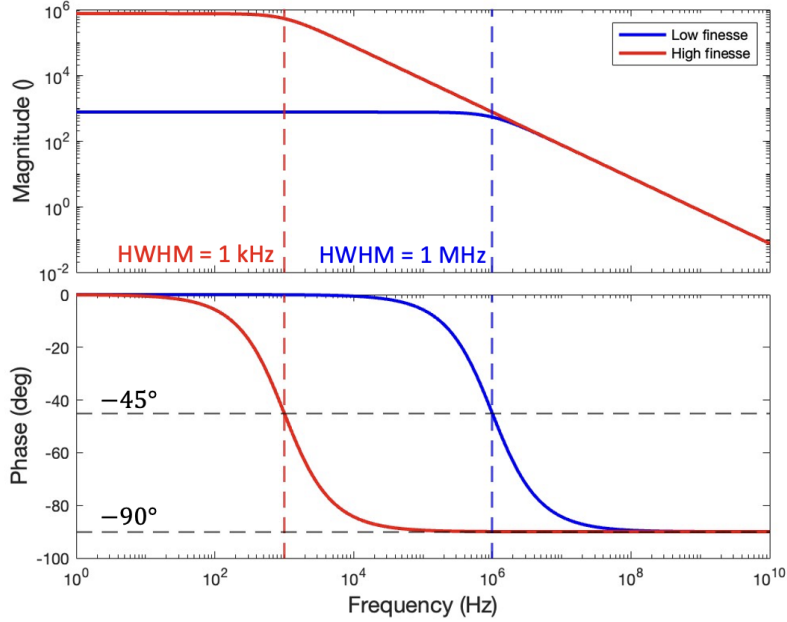
Figure 25: Frequency responses of the PDH technique for a low-finesse cavity (blue) and a high-finesse cavity (red). The response is a low-pass filter with a corner frequency at the HWHM of the cavity.

The corner frequency happens at the HWHM of the cavity, which is inversely proportional to the finesse. At this frequency, the magnitude decreases to $1/\sqrt{2}$ and the phase lag is $45°$. The total phase lag of the PDH technique at this frequency is $90°$.

The gain, on the other hand, is proportional to the finesse. For a high-finesse cavity, the average time inside the cavity is longer. This results in a better signal-to-noise ratio, and therefore a higher gain.

Based on different cavities, we can choose the suitable controller as illustrated in Figure 26. For low-finesse cavities used to stabilize the lasers driving dipole transitions, the roll-off happens at HWHM$\approx 1\,\mathrm{MHz}$, which is a lot larger than the required loop bandwidth of $1\,\mathrm{kHz}$. Therefore, the frequency response of the PDH technique can be treated as completely flat. Since the actuator is also flat, we only need an integral controller to get the desired shape of the loop gain.

However, in the high-finesse domain for quadruple transition at 729 nm, the PDH technique has a lower roll-off frequency due to the smaller cavity linewidth. Since we want a feedback loop bandwidth of more than 1 MHz, the frequency response behaves as a low-pass filter, hence we could use a PI controller to shape the loop gain.

Integrator loop gain
L(s)=

Fast detector
H(s)=

Slow detector

Fast actuator
P(s)=

Slow actuator

Fast actuator

Slow actuator

I controller

PI controller

PI controller

PID controller

Low finesse cavities with a
target bandwidth of ~1 kHz

High finesse cavities with a
target bandwidth of ~1 MHz
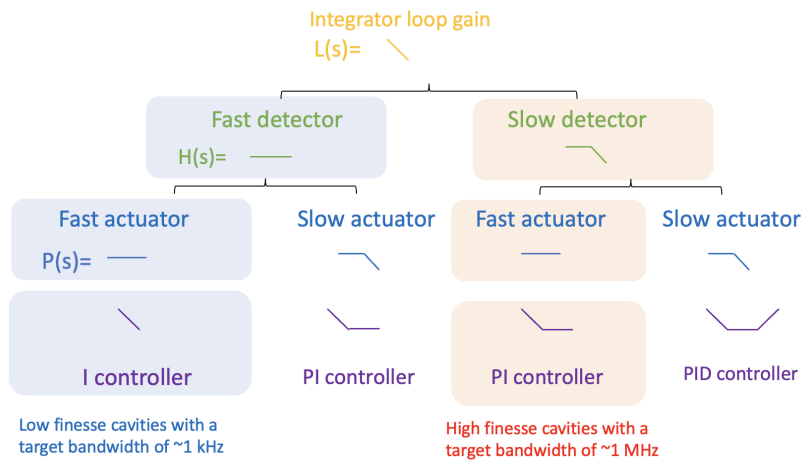
Figure 26: Choosing the suitable controller based on cavities and targeted loop bandwidth. The low-finesse cavity has a flat response in the desired lock bandwidth, so an integrator-only controller is needed. The high-finesse cavity behaves as a low-pass filter for much larger bandwidth, so a PI controller is needed.

## 3.4   Low-finesse cavities
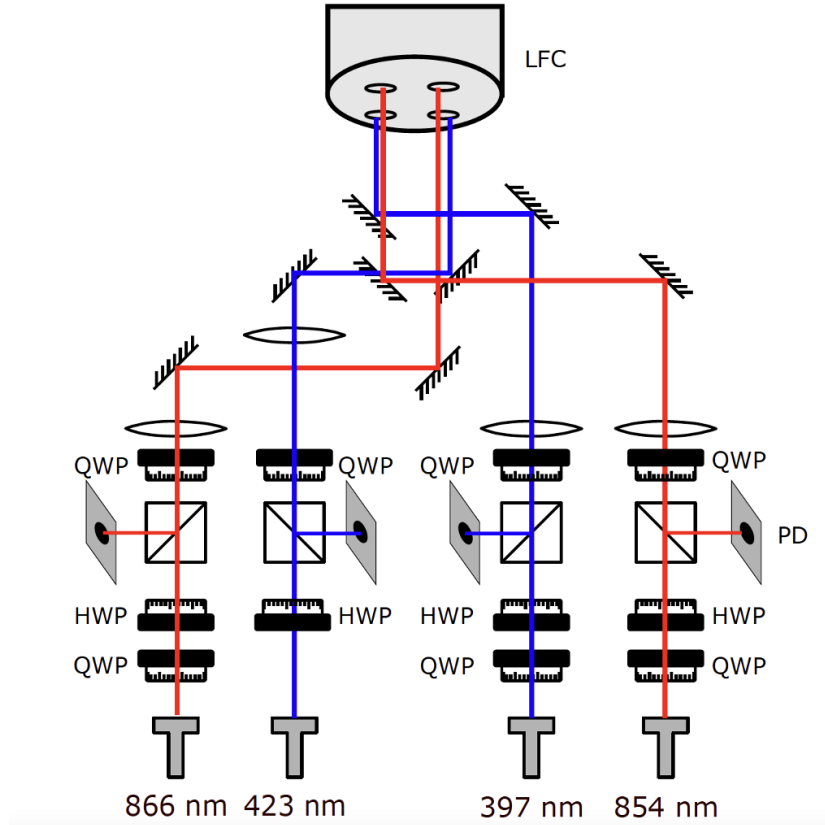


Figure 27: Low-finesse cavities optics setup. Elements not shown are the fiber EOMs before the fiber collimators and the cameras after the cavities.

The setup for the lasers at 866 nm, 423 nm, 397 nm, and 854 nm involves using 4-bore low-finesse cavities from Stable Laser Systems (SLS). The optics arrangement is depicted in Figure 27. The laser light is modulated either by a fiber EOM or by the laser current. The modulated light then passes through a quarter-wave plate (QWP) and a half-wave plate (HWP). This linearly-polarized light is transmitted through a polarizing beam splitter (PBS) and further passes through a second QWP to become circularly polarized. The beams are then coupled to the cavities that are enclosed in a vacuum chamber.

The reflected light passes through the QWP again to become linearly polarized in the opposite direction. The light is then reflected by the PBS and captured by the photodiode (PD). The actual setup and the corresponding error signal are illustrated in Figure 28.

(a)                                          (b)
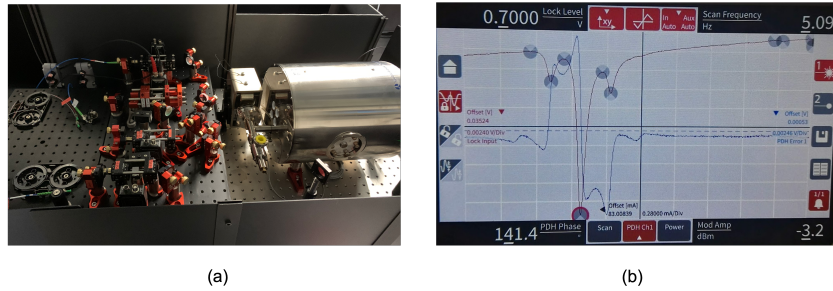
Figure 28: (a) Actual optics setup of the low-finesse cavities; (b) cavity reflection signal (red) and the PDH error signal of one of the lasers (blue).

## 3.5   High-finesse cavities

High-finesse cavities are used to lock the 729 nm lasers. The optics setup for a high-finesse cavity is very similar to the low-finesse ones and is illustrated in Figure 29. A difference is that instead of HWP + PBS in the low-finesse setup to split the directions of the incident and reflected light, a Wollaston prism is used. The prism uses the birefringence property that gives different indices of refraction for differently linearly polarized light, thus separating the two orthogonally polarized beams.
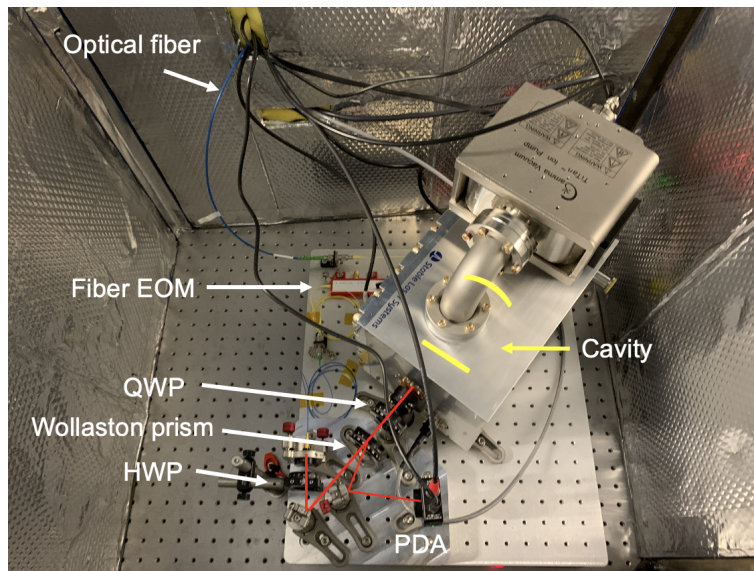


Figure 29: Optical setup of a high-finesse cavity. The elements are very similar to the low-finesse cavities as in Fig. 27, except the separation of the incoming and reflected beam paths is done with a Wollaston prism.

The system needs to be very stable since any noise in the cavity can cause frequency drift of the locked laser. Acoustic and electromagnetic interference (EMI) shielding, as well as an active vibration isolation system, are added to reduce the noise. The system also features temperature control. Ultra-low expansion glass (ULE), which has a quadratic dependence on temperature, is used as a spacer between the mirrors [2]. At zero-crossing temperature $T_c$, the ULE has a minimum thermal expansion that causes minimum frequency drift.

After coupling light to the cavity, different resonator modes can be found by scanning the laser frequency through the piezo voltage. At the beam waist, the mode can be Gaussian (TEM 00) or higher-order Hermite-Gaussian modes. The spacing between the two same modes is the free-spectral range of 1.5 GHz. An example of the resonator mode separation of high-finesse cavity B is shown in Figure 30. Since the cavity's TEM 00 mode is different from the qubit transition frequency, AOMs are needed to bridge the frequencies for qubit manipulation.
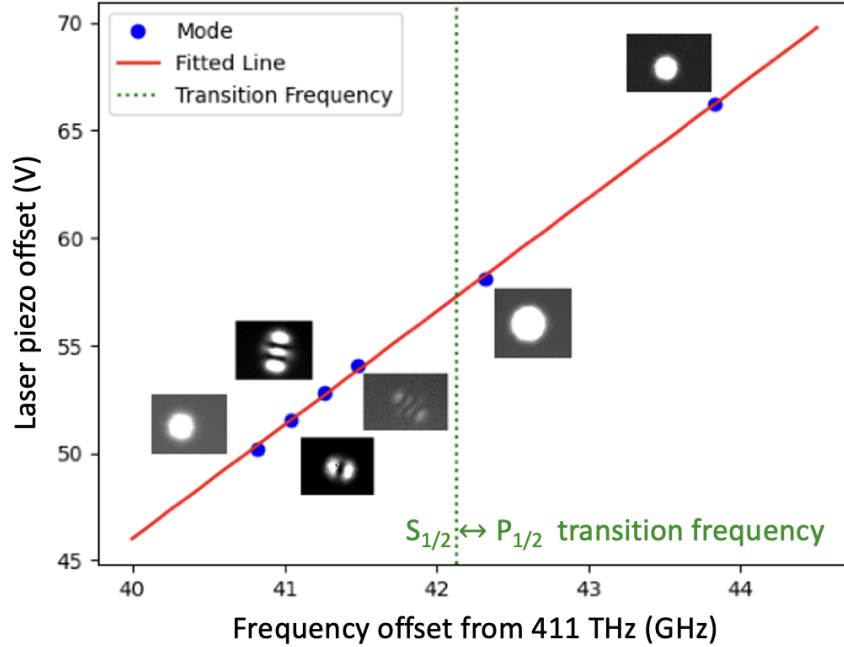


Figure 30: Resonator modes of the high-finesse cavity B. The 729 nm laser will be locked to one of the TEM 00 modes, where additional AOMs are required to bridge the frequency difference between the cavity mode and the qubit transition frequency.

# 4 Closed-loop characterizations of 729 nm lasers

## 4.1 TOPTICA lasers

### 4.1.1 System overview

The lab layout of the TOPTICA laser system is illustrated in Figure 31. Two 729 nm lasers are incorporated in a TOPTICA rack. Each laser system comprises an ECDL followed by a TA, collectively referred to as the MTA pro. For detailed layout of the MTA pro system, please refer to Figure 9. Inside the ECDL, there is an intra-cavity EOM for fast adjustment of laser frequency, which is not a common feature in typical lasers.

The amplified light from laser rack is split out on a neighboring table, where less than 1 mW of the light is delivered to the cavity through optical fibers. The cavities are housed inside acoustic enclosures. The reflected signals are sent to the controllers in the rack through coaxial cables.
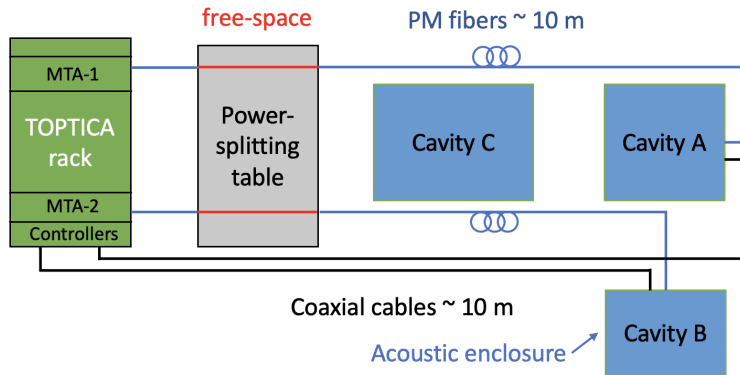


Figure 31: Layout of the TOPTICA 729 nm laser system. The laser light is split and then sent to the high-finesse cavities through polarization maintaining (PM) fibers. The RF signal from the cavity reflection is sent to the controllers inside the rack.

### 4.1.2 Setup for closed-loop characterization

The actual loop diagram for closed-loop characterization is shown in Figure 32. The sensing part $H_{\mathrm{PDH}}$ is the PDH error generation technique, the controller $C_{\mathrm{FALC}}$ is FALC pro and the actuator $P_{\mathrm{EOM}}$ is the intra-cavity EOM. For a detailed instructions on closed-loop characterization from the measurement, please refer to Section 2.4. This feedback loop differs from Figure 17 in that, due to the inner design of the controller, the real summing junction has a 20-dB attenuator. Therefore, a renormalization of $S(s)$ and $T(s)$ are required.
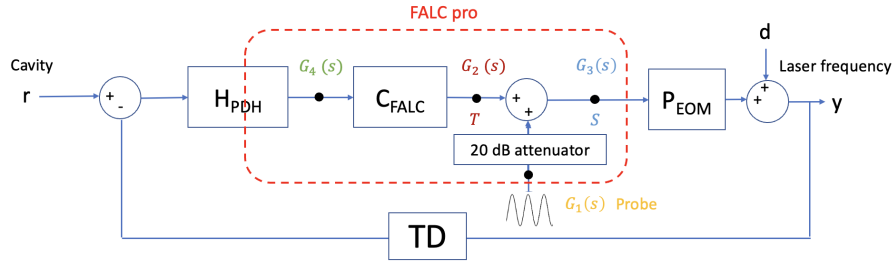
Figure 32: Loop diagram of the MTA-Cavity system. Different from the conceptual diagram in Figure 17, the real summing junction has a 20-dB attenuator, so re-normalization of $S(s)$ and $T(s)$ with an open-loop measurement is required.

The characterization is done by connecting the Analog Discovery Pro: ADP3450 to the feedback loop, as illustrated in Figure 33. On the FALC pro, the "Main offset" features an unused summing junction that can be utilized for signal injection, denoted as $G_1(s)$. The "Main" port, located after the summing junction, detects $G_3(s)$. The "Mon" port provides two distinct measurements: When setting Mon=0, the output measures the signal before reaching the controller, namely $G_4(s)$. When Mon=1, the output measures the signal after the controller but before the summing junction, which corresponds to $G_2(s)$.
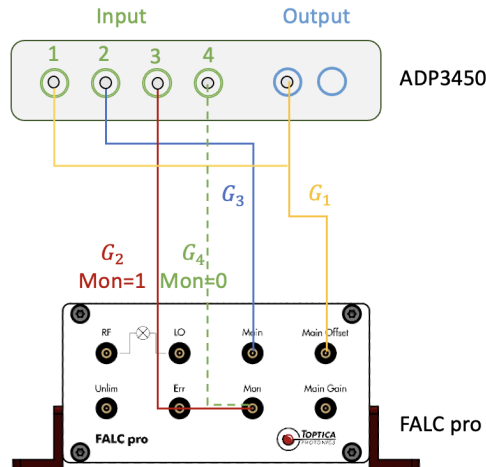


Figure 33: Cable connections of the closed-loop characterization. The ADP3450 is connected to FALC pro for signal injection and frequency response measurement. Both $G_2$ and $G_4$ can be accessed via the port "Mon" by changing the internal settings on FALC pro.

### 4.1.3  Results of closed-loop characterization

**Controller**

First, we can obtain the frequency response of the controller from $G_2(s)/G_4(s)$. The data is then fitted into a model of PI controller:

$$C_{\mathrm{PI}}(s) = G_{\mathrm{HF}} \cdot \frac{1 + \frac{\omega_z}{s}}{1 + \frac{\omega_p}{s}} \tag{29}$$

where $\omega_z$ is the upper corner frequency $330\,\mathrm{kHz}$ and $\omega_p$ is the lower corner frequency at $470\,\mathrm{Hz}$ set on the controller; $G_{\mathrm{HF}}$ is the gain at high frequency. The measured and fitted curves are shown in Figure 34.
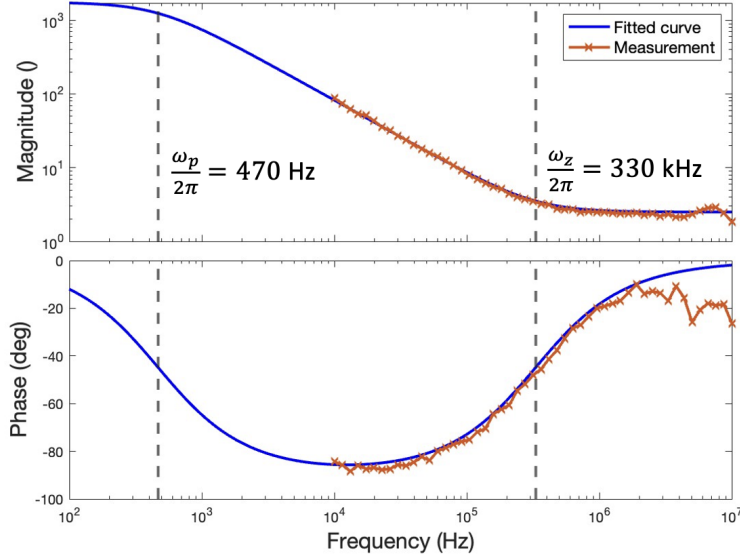


Figure 34: Measured and fitted curves for the controller FALC-1. It is a limited PI controller with a lower corner frequency at $470\,\mathrm{Hz}$ and an upper corner frequency at $330\,\mathrm{kHz}$.

**L, S and T**

The measurements of $S(s)$ and $T(s)$ (after re-normalization) are plotted in Figure 35. As expected, $S(s)$ attenuates disturbance and $T(s)$ follows the reference effectively at low frequencies. At 240 kHz, the peaking (servo bump) appears, which is a coarse estimate of the lock bandwidth.
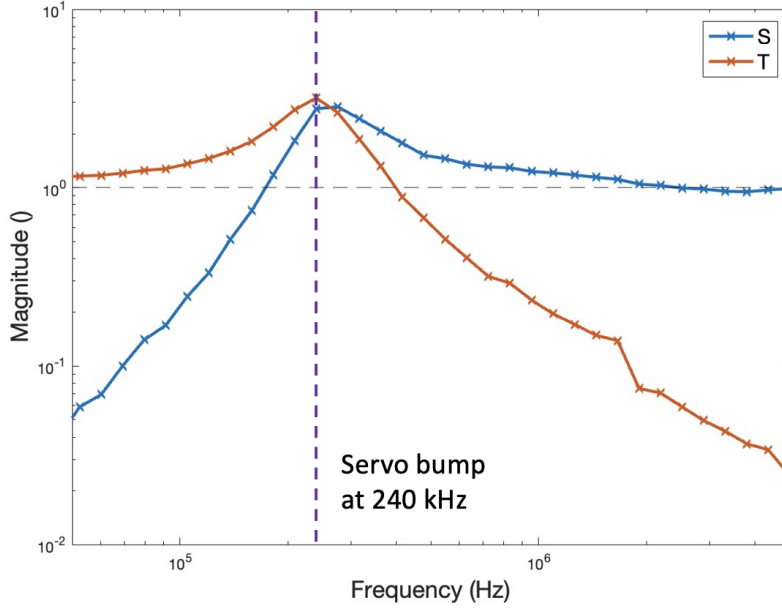
Figure 35: $S(s)$ and $T(s)$ of the closed-loop characterization of the PDH laser frequency stabilization loop, locking the TOPTICA MTA1 to high-finesse cavity A. The servo bump at approximately 240 kHz gives an estimation of the locking bandwidth.

From $S(s)$ and $T(s)$, we can infer the loop gain $L(s)$ by Eq.11. We performed a manual fit of the curve to match the inferred loop gain

$$L_{\text{fit}}(s) = g_0 \cdot H_{\text{PDH}}(s) \cdot C_{\text{PI}}(s) \cdot P_{\text{EOM}}(s) \cdot TD(s) \tag{30}$$

where $g_0$ is an arbitrary gain, $H_{\text{PDH}}(s) = \frac{1}{1+s/\omega_{\text{HWHM}}}$, and $C_{\text{PI}}(s)$ is the controller in Eq.(29). The unknowns are the actuator's response $P_{\text{EOM}}(s)$ and the time delay $TD(s) = e^{-s\tau}$. We found that the measurements are described well by using $P_{\text{EOM}}(s) = $ flat and TD= 190 ns, as visible in Figure 36. The fitted curve $L_{\text{fit}}(s)$ nicely coincides with the experimentally inferred loop gain $L(s)$.
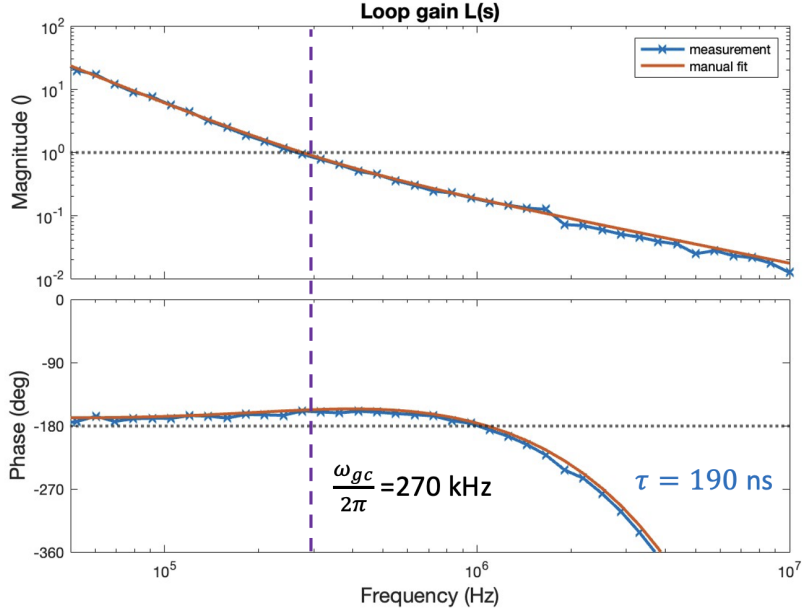
Figure 36: Inferred loop gain from $S(s)$ and $T(s)$. The gain crossover happens at 270 kHz. A manual fit was performed to find a time of about 190 ns.

At the gain crossover frequency of 270 kHz, the phase margin is only 24°. This suggests that the time delay, corresponding to a cable length of approximately 38 m, limits the locking bandwidth. The cable length primarily includes a 10 m optical fiber extending from the laser rack to the cavity, and another 10 m coaxial cable running from the cavity back to the laser rack, as illustrated in Figure 31. The fiber EOM inside the acoustic enclosure also contributes approximately 6 m to the overall cable length.

The consistency of the fitted curve with the inferred loop gain also confirms that the frequency response of the intra-cavity EOM is perfectly flat. The EOM contributes negligible roll-off and phase lag within the lock bandwidth.

### 4.1.4 Discussion of results

**Control design**

For the current system, it is desirable to lower the upper PI corner frequency from 330 kHz to 150 kHz for better stability and robustness[2]. The gain is then adjusted such that the gain crossover frequency is about 400 kHz, which leads to an improved phase margin of 43° compared to the 24° we had previously.

The DC responses of the actuators are shown in Table 4. While the EOM alone can keep the laser locked over time scales of seconds to minutes, it even-

---

[2]In the Toptica FALC pro, we have correspondingly also lowered the corner frequency of I2 from 470 Hz to 220 Hz for it to seamlessly extend I1.

tually reaches the end of its travel range. In order to extend the lock essentially indefinitely, we therefore additionally use a slower actuator (laser current or laser piezo) to relieve the EOM. These slower actuators have a larger travel range, making them suitable for counteracting slow drifts like in Figure 4. We drive the slow actuator with an integral-only controller.

| Actuator | Sensitivity | Allowed control voltage | Travel range |
|----------|-------------|-------------------------|--------------|
| EOM | 1.1 MHz/V | ±3.7V | ±4 MHz |
| Current | −140 MHz/mA | - | essentially infinite |
| Piezo | 150 MHz/V | - | essentially infinite |

Table 4: DC responses of TOPTICA actuators.

In practice, we have found it beneficial to alter the topology of the feedback loop compared to what the manufacturer of the laser and controller suggests: Instead of feeding the controller of the slow actuator directly based on the PDH error signal, we feed it with the control signal sent to the EOM, as illustrated in Figure 37. This makes it much easier to adjust the voltage offsets and prevents the occurrence of destructive interference between the slow and the fast actuator that we encountered using the scheme suggested by the manufacturer. For a detailed discussion of an analogous case see [17, pp.135 ff and pp.185 ff].
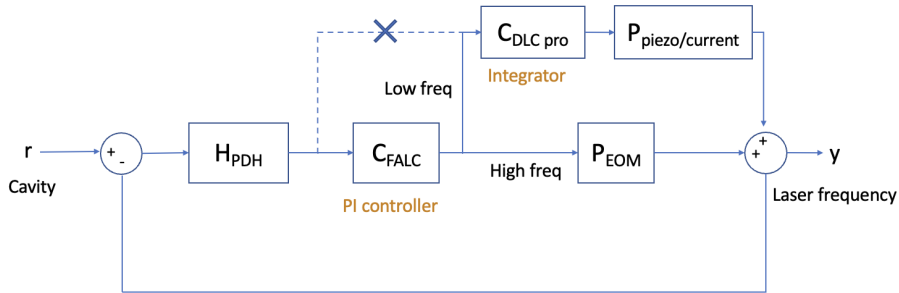


Figure 37: Overall control design including both the fast and the slow actuators. In practice, we have found it to be beneficial to use the control signal sent to the EOM as the input for the controller of the slow actuator. Because the secondary controller of the FALC pro used here is hard-wired to use the PDH error signal as its input, we instead use one of the PID controllers of the DLC pro in order to form the slow feedback loop and use the control signal sent to the EOM as its input.

**Overall system re-design**
The main takeaway from the closed-loop characterization of the feedback loop is that its bandwidth is currently limited to about 500 kHz due to time delays of about 200 ns due to signal propagation in coaxial cables and optical fibers.

This is quite unfortunate, as the intra-cavity EOM has a nice and flat response that in principle would allow for much larger bandwidths.

In practice, realizing the allowed bandwidths would require drastic changes to the setup, which means a complete re-arrangement of the laboratory for minimizing the time delays. We estimate that at best we could reduce them down to about 20 ns, which would allow the bandwidth of the feedback loop to be increased up to about 5 MHz, see Eq.(4). However, given the noise of the free-running laser, this is probably still insufficient to cleanly implement two-qubit gates.

Accordingly, additional measures to further clean up the optical spectrum of the laser would be required, such as spectral filtering with a cavity [1] or feedforward schemes [13].

## 4.2 MSquared Laser

### 4.2.1 System overview

The setup of the MSquared Ti:Sa laser with the high-finesse cavity C is shown in Figure 38. The laser sits on one optical table and its light is delivered to the optical cavity on another optical table via an optical fiber. The error signal is sent to the Vescent D2-125 controller through a coaxial cable, and the controller's output is sent to the actuators.

We use the Vescent controller because it features two advantages that makes the initial characterization convenient. First, in contrast to FALC controller, the Vescent controller allows for an unlimited integrator range, enabling the laser to be locked with the intra-cavity EOM alone. Additionally, the output voltage of the Vescent controller is $\pm 10\,\mathrm{V}$, which is more than twice the range of the FALC controller. This enables the EOM to operate within its maximum range.
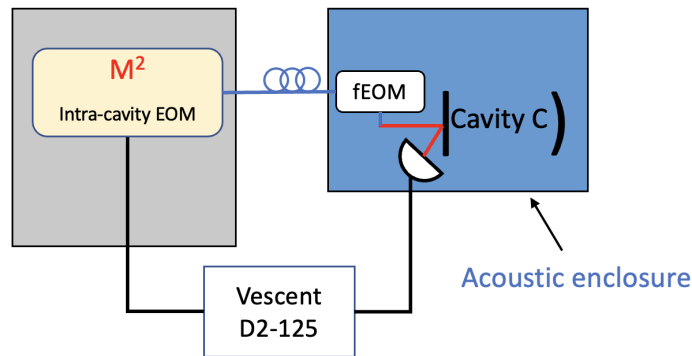


Figure 38: Layout of the MSquared-Cavity system. Light from the MSquared laser is delivered to the high-finesse cavity C. The reflected signal is sent to the Vescent controller, and the controller's output is sent to the laser's actuators.

### 4.2.2 Setup for closed-loop characterization

The loop diagram for closed-loop characterization is illustrated in Figure 39. Since the system lacks a summing junction like FALC pro, we use the New Focus LB1005 for signal injection.
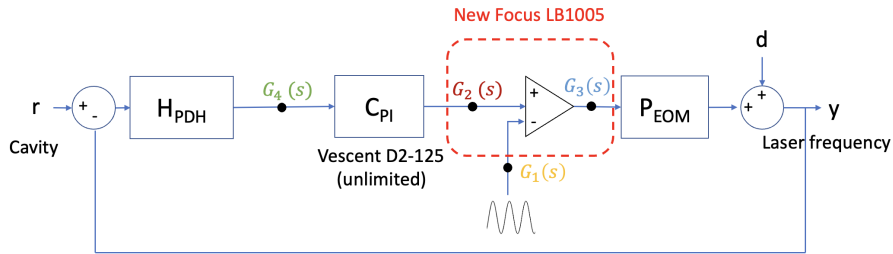
Figure 39: Loop diagram of the MSquared-Cavity system. The New Focus box provides a fast summing junction for signal injection.

### 4.2.3   Results of closed-loop characterization

The closed-loop measurement results of the MSquared laser are mostly the same as TOPTICA lasers. Figure 40 shows the behavior of $L(s), S(s)$ and $T(s)$. The gain crossover happens as $450\,\text{kHz}$, and a time delay of $140\,\text{ns}$ limits the achievable gain crossover frequency.
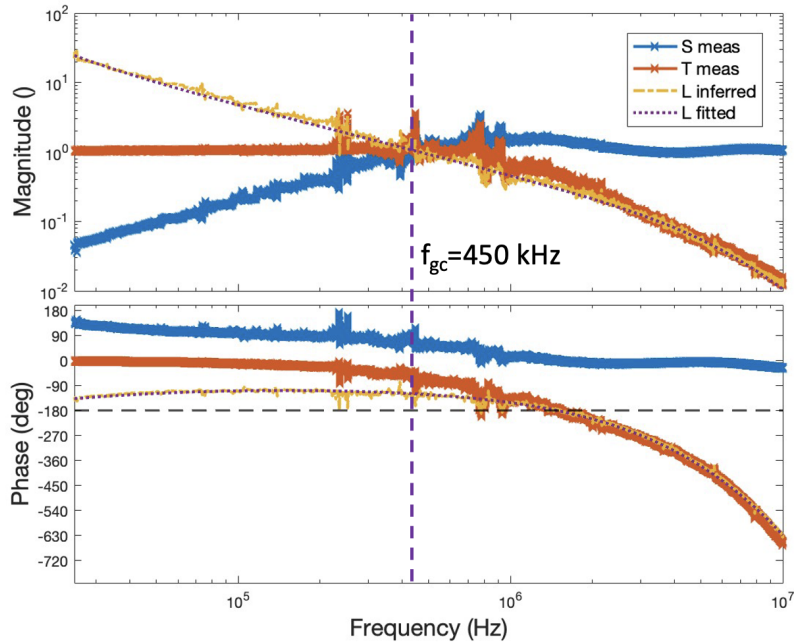


Figure 40: Results of the closed-loop characterization of the PDH laser frequency stabilization loop, locking the MSquared laser to high-finesse cavity C.

Additionally, in Figure 40, the loop gain between 200 kHz and 1 MHz shows significant wiggles. These are due to mechanical resonances of the EOM crystal getting excited by the drive voltage: Thanks to the electro-optic effect, the applied voltage leads to a phase shift of the light passing through the crystal as desired. However, EOM crystals are typically also piezo-electric, meaning that the applied voltage also excites the crystal mechanically. At the mechanical resonances of the EOM crystals, these excitation become large. In turn, these undesired mechanical excitation alter the phase shift experienced by the laser beam unfavorably [11].

The EOM frequency response can be calculated by

$$P_{\mathrm{EOM}}(s) = \frac{L_{\mathrm{measured}}(s)}{g_0 \cdot H_{\mathrm{PDH}}(s) \cdot C_{\mathrm{PI}}(s) \cdot TD(s)} \tag{31}$$

and is plotted in Figure 41.
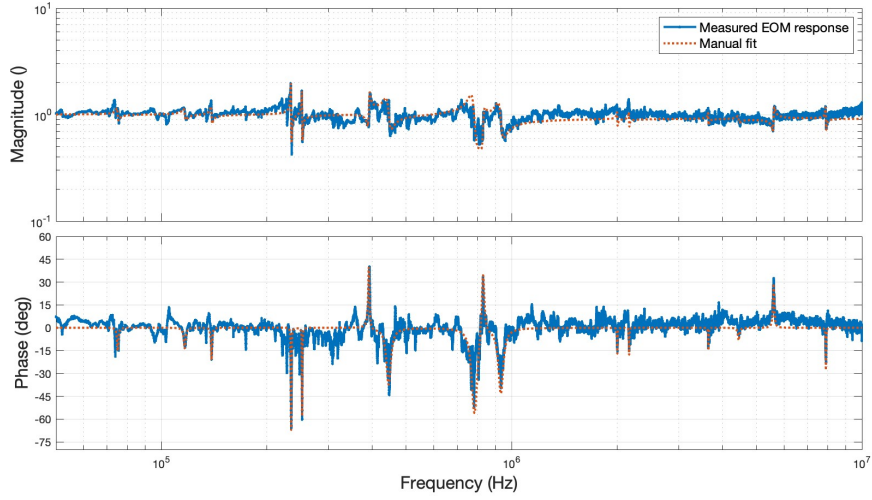


Figure 41: Frequency response of the intra-cavity EOM of the MSquared laser inferred from the closed-loop measurements from Figure 40. A coarse manual fit with a few mechanical modes is shown for illustrative purpose. Main resonances happen at 235 and 252 kHz, 445 kHz, 782, and 930 kHz. The phase drops by up to 70° endangers the stability of the feedback loop.

The instability of the feedback loop resulting from the EOM resonances can be observed directly in Figure 42. Here, the gain crossover frequency approaches one mechanical resonance at 235 kHz, where the phase drop causes strong oscillations of the feedback loop.
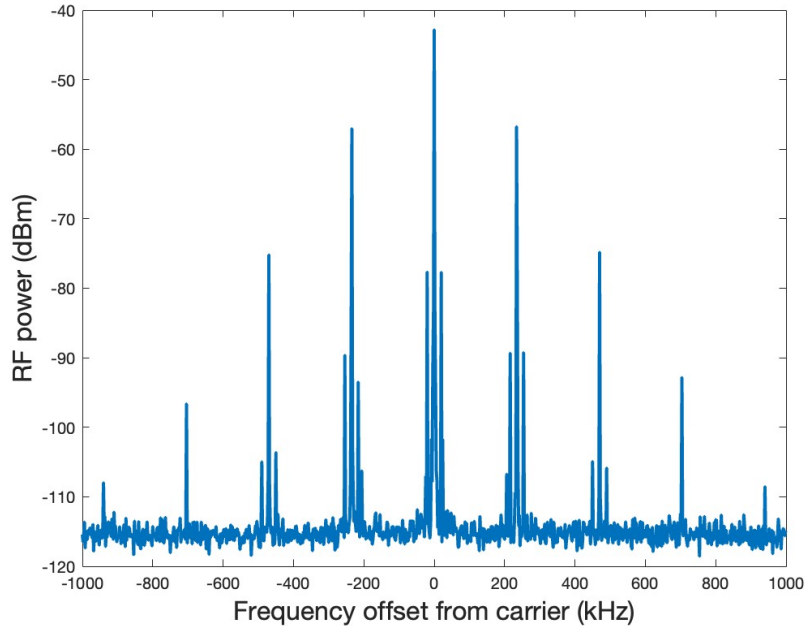
Figure 42: Beatnote measurement of the laser light before and after the cavity. The feedback loop is oscillating with a EOM resonance at 235 kHz.

### 4.2.4 Discussion of results

**Control design**

The gain crossover of the laser frequency stabilization loop is currently limited to about 70 kHz due to the presence of strong narrowband resonances in the response of the intra-cavity EOM (see Fig. 41). At these resonances, the phase drops sharply by up to 70°, endangering the stability of the feedback loop by eating away the phase margin. In principle, it is possible to push the gain crossover to a few hundred kilohertz. In practice, doing so is very risky, as the stability and robustness margins of the resulting feedback loop are then exceedingly poor. The feedback loop is then prone to break into oscillation at the slightest whim, which matches our practical experiences in the lab. This is especially insidious, as a cursory look at the usual diagnostics such as the cavity transmission still indicates the laser to be locked as usual, and only more refined diagnostics such as the error signal spectrum or the laser spectrum reveal the presence of these oscillations.

For now, we have opted to stay out of the mine-field constituted by the EOM resonances, and have gone for a "slow and safe" control design, as illustrated in Figure 43 a). As shown, the loop gain $L(s)$ has its gain cross-over already at 70 kHz, which is well below the first strong EOM resonances that occur at 235 kHz and 252 kHz. This results in a safe (meaning stable and robust) albeit

slow lock. From theory, we expect the frequency noise PSD of the free-running laser to have a broad peak at around 100 kHz, corresponding to the relaxation oscillations of the Ti:Sa laser. Unfortunately, the slow and safe lock is unable to counteract them, motivating us to look for a better solution.

In the future, we want to go to a "fast and safe" control design, as illustrated in Figure 43 b). The careful characterization of the EOM (see Fig. 41) showed that there are no strong resonances above 1 MHz. If we could push the gain crossover frequency to well above that, the EOM resonances could be tolerated, since they then occur in the frequency region where the loop gain is still well above unity. They then only lead to minor local degradations of the disturbance attenuation but no longer endanger the stability and robustness of the overall feedback loop, thus leading to a "fast and safe" lock. Currently, the time delays of about 140 ns prevent us from accessing this regime. However, by moving the laser right next to the high finesse cavity it is locked to, we should be able to reduce the time delays sufficiently to access this operating regime.
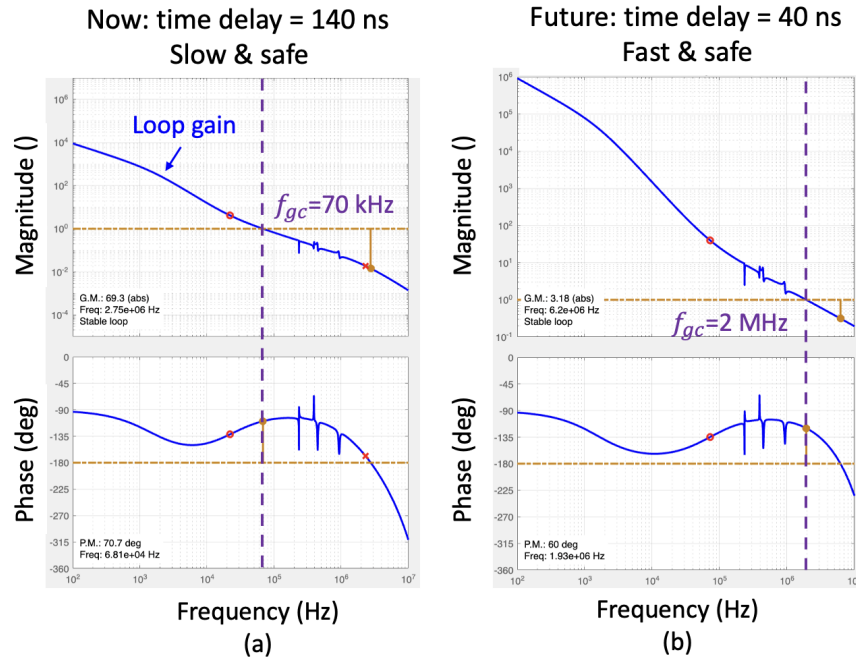


Figure 43: Bode plots of loop gain for the MSquared Ti:Sa laser using the intra-cavity EOM as the fastest actuator. a) Currently used control design where the gain crossover is intentionally placed well below the first EOM resonance in order to get a "slow and safe" lock. b) Envisioned future control design where the gain crossover is pushed to be well above the highest EOM resonance occurring at 932 kHz, resulting in a "fast and safe" lock.

Quickly relieving the EOM with the fast piezo is also crucial in practice

due to the very limited travel range of the intra-cavity EOM (see Table 5). Specifically, when using the EOM alone, we found that the lock only lasts for a few seconds. Additionally, the control signal sent to the EOM to counteract the noise of the free-running laser essentially occupies its full ±10 volt span. For the "fast and safe" design above, we intend to use the FALC pro as the fast controller, as its time delay is only about 10 ns compared to the 25 ns of the Vescent D2-125. However, in contrast to the Vescent D2-125, the fast control output of the FALC pro can only go up to ±3.7 volts instead of ±10 volts. This necessitates pushing the hand-over frequency where the fast piezo takes over control action from the EOM up to about 15 kHz, as most of the strong laser frequency disturbances occur at 1.5 kHz and below. Based on preliminary tests and a detailed characterization of the fast piezo from [17, Figure 9.5], we determined this to be feasible.

| Actuator | Sensitivity | Allowed control voltage | Travel range |
|---|---|---|---|
| Intra-cavity EOM | $50\,\text{kHz/V}$ | $\pm 10\,\text{V}$ | $\pm 500\,\text{kHz}$ |
| Fast Piezo | $2.6\,\text{MHz/V}$ | $\pm 10\,\text{V}$ | $\pm 26\,\text{MHz}$ |
| Slow Piezo | $2\,\text{GHz/V}$ | $\pm 10\,\text{V}$ | $\pm 20\,\text{GHz}$ |

Table 5: DC responses of MSquared actuators.

As the fast piezo also has a limited travel range, it in turn will have to be relieved by the slow piezo on long time scales. In practice, we have found it sufficient if this hand-over is performed on slow timescales, allowing it to be implemented in software by occasionally sending commands to the controller of the Ti:Sa laser over the network. This is useful, as it requires no additional hardware, can be controlled remotely, and frees us from having to deal with issues such as ground loops that would occur if this loop were implemented with analog electronics.

The full scheme combining all three actuators is shown in Figure 44, and the division of the corrective actions over the various frequency ranges is illustrated in Figure 45.
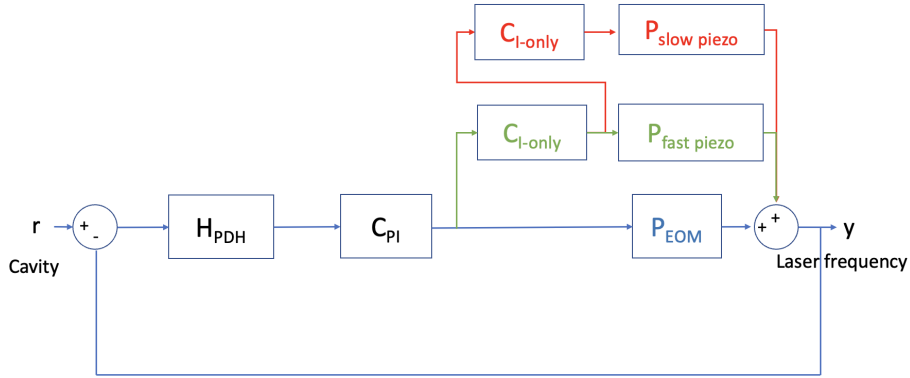
Figure 44: Control design for the full feedback loop combining all three actuators: The intra-cavity EOM, the fast piezo, and the slow piezo. The hand-over between the EOM and the fast piezo should be at around 15 kHz in order to preserve the travel range of the EOM. The hand-over between the fast and the slow piezo can be at 1 Hz or slower, allowing the controller of the slow piezo to be implemented in software. Note that here we again use the topology from Figure 37 with its attendant benefits discussed there.
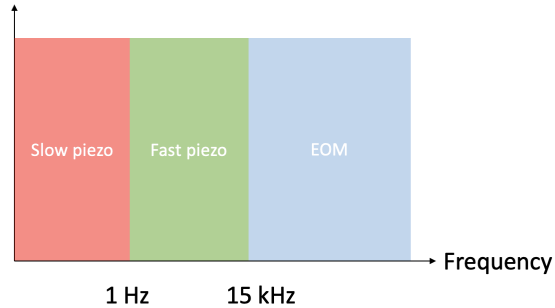


Figure 45: The frequency ranges covered by the three actuators. The EOM handles the fastest frequency fluctuations and is relieved by the fast piezo at around 15 kHz. The fast piezo in turn is relieved by the slow piezo at around 1 Hz or below.

### 4.2.5   Conclusions

We have performed a closed-loop characterization of the feedback loop stabilizing the frequency of the Ti:Sa laser to a high-finesse cavity. Similar to the diode lasers treated in section 4.1, we have found time delays to limit the bandwidth of the feedback loop. However, the presence of undesired piezo-acoustic

resonances of the EOM forced us to further limit the bandwidth of the feedback loop to about 70 kHz for safe and robust day-to-day operations.

Informed by these findings, we have re-designed the system. Specifically, we have decided to move the laser into the acoustic enclosure that also houses the high-finesse cavity, as illustrated in Figure 46. Doing so reduces the time delays, and should allow us to increase the bandwidth of the feedback loop to a few Megahertz. This in turn should allow for a "safe and fast" lock that avoids the EOM resonances. Furthermore, it should also allow us to suppress the frequency noise peak at the relaxation frequency that is expected to be around 100 kHz. As the frequency noise PSD of the free-running laser should roll off rapidly above that (see Fig. 5), this should allow us to then cleanly drive both single- and two-qubit gates without requiring any additional measures. The re-designed system is currently being built in the laboratory and construction is already well underway.
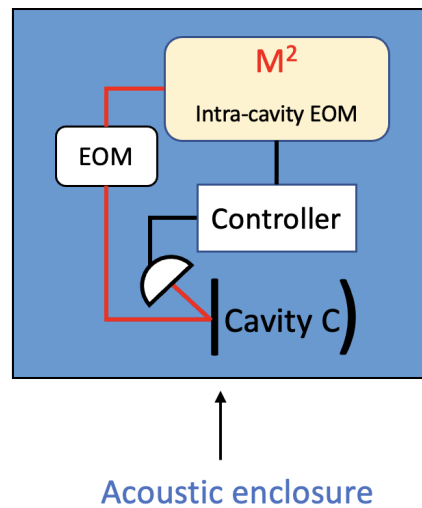


Figure 46: New arrangement of the MSquared laser setup. To reduce time delay, the laser is moved inside the acoustic enclosure (blue) housing the cavity, and the fiber EOM is replaced with a free-space EOM. The rearrangement will enable the "fast and safe" control design.

# 5 Preliminary characterizations of the frequency noise of the locked lasers

As discussed in section 1.2.2, cleanly implementing single and two-qubit gates requires not only a narrow linewidth, but also a clean optical spectrum around the narrow central peak. In terms of the laser frequency noise PSD, this means that the PSD at offset frequencies between a few hundred kilohertz up to a few megahertz, corresponding to the typical ion trap motional frequencies, should also be kept low. In chapter 4 we performed an in-depth characterization of the disturbance attenuation $S(s)$ achievable with a feedback control loop. However, the laser frequency noise PSD of the locked laser $S_{\Delta\nu}^{\mathrm{locked}}(f)$ (in $\mathrm{Hz}^2/\mathrm{Hz}$) is given by[3]

$$S_{\Delta\nu}^{\mathrm{locked}}(f) = S_{\Delta\nu}^{\mathrm{free}}(f) \left| S(f) \right|^2 \tag{32}$$

where $S_{\Delta\nu}^{\mathrm{free}}(f)$ denotes the frequency noise PSD of the free-running laser. In the end, we are primarily interested in $S_{\Delta\nu}^{\mathrm{locked}}(f)$, and the disturbance attenuation $S(f)$ is therefore only one-half of the coin.

## 5.1 Methods to measure $S_{\Delta\nu}^{\mathrm{locked}}(f)$

Here, we have considered three different methods to measure $S_{\Delta\nu}^{\mathrm{locked}}(f)$ based on:

1. the spectrum of the in-loop PDH error signal

2. a beat note between light before and after the high-finesse cavity used for PDH error signal generation

3. beat notes between three independent narrow-linewidth laser systems (i.e. a three-cornered hat measurement)

A comparison of the frequency ranges where these three methods are applicable is presented in Figure 47. As illustrated, the first method based on the in-loop error signal works over the full frequency range but can be unreliable at times. Specifically, the feedback loop typically works hard to null the error signal regardless of whether the said error signal is actually accurate or not. For example, in case there is a lot of measurement noise, a high-gain feedback loop will simply imprint the measurement noise onto the laser frequency to null the error signal. The second method is comparably easy to implement but only works well above the cavity HWHM (about 3 to 4 kHz in our case) where the cavity filters phase noise well. There, the cavity transmission can therefore serve as a near-ideal reference beam. The third method involving the three-cornered hat measurement works over the full frequency range but is also the hardest to perform in practice, as it requires three independent narrow-linewidth laser systems.

---

[3]For convenience, here we assume the frequency reference to be perfectly stable and also neglect measurement noise.

So far, we have made preliminary measurements with the first two meth-
ods, which yielded comparable results. We are currently also working towards
implementing the three-cornered hat measurement.
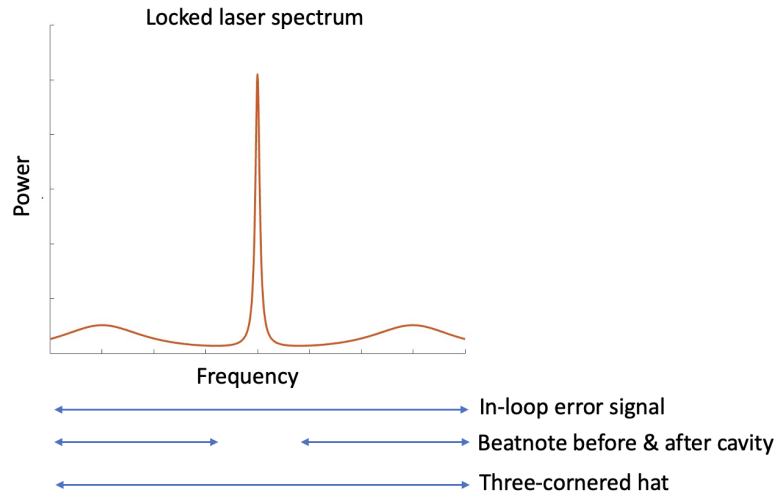


Figure 47: Conceptual illustration of the optical spectrum of the locked laser,
and the frequency ranges where the three methods to measure the frequency
noise of the locked lasers yield reliable results.

## 5.2 Preliminary results based on an optical beat note between light before and after the cavity

Here we present the first preliminary results obtained using a beat note between light before and after the cavity. The experimental setup is presented in Figure 48, and the resulting optical beat notes that were recorded on a fast photodiode are shown in Figure 49.
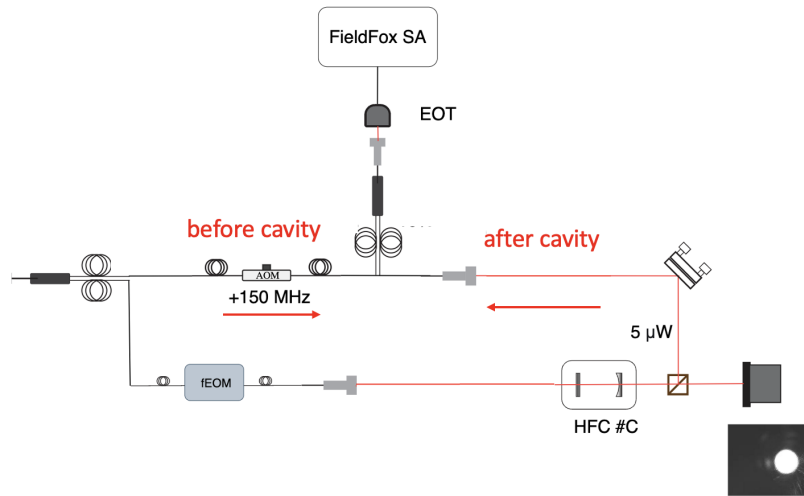


Figure 48: Experimental setup used to measure the frequency noise of the locked laser via an optical beat note between light before and after the cavity. The light before the cavity is shifted by 150 MHz using an AOM. The light going through the cavity is spectrally filtered by it, resulting in a near-ideal reference at offset frequencies well above the cavity HWHM. The cavity transmission was coupled into a fiber and then combined with light before the cavity using an in-fiber power splitter/combiner. The resulting beat signal was directed onto a fast photodiode whose signal was then recorded with a spectrum analyzer.
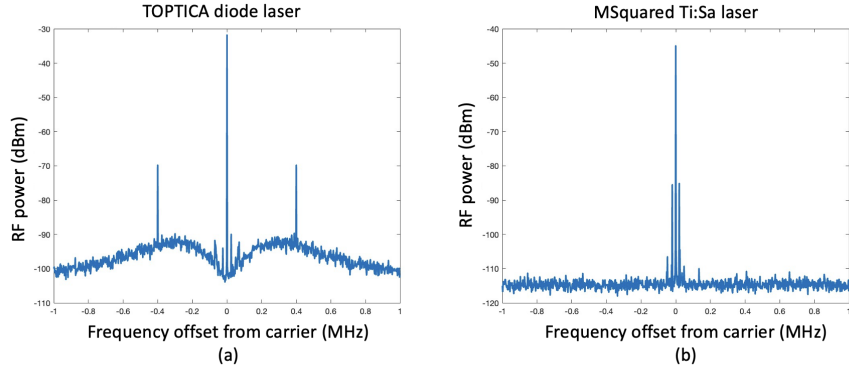
Figure 49: Results of the measurement of a beat note between the light before and after the cavity. a) Results for the system based on an ECDL (RBW = VBW = 300 Hz). b) Results for the system based on a Ti:Sa (RBW = VBW = 30 Hz).

In the case of the system based on the ECDL, as shown in Fig 49a), we see a narrow central line, with broad side-lobes peaking at a frequency offset of about ±300 kHz away from the carrier. This corresponds to the peaking in the disturbance attenuation $|S(s)|^2$ above the gain-crossover frequency (see Fig. 35), which results in the frequency noise PSD of the free-running ECDL getting amplified instead of attenuated.

In contrast, the optical beat note recorded with the system based on the Ti:Sa laser shown in Fig. 49b) primarily features a narrow central peak and a few side peaks at frequency offsets of ±19.4 kHz (and its odd harmonics) corresponding to the etalon lock modulation frequency. In contrast to the system based on the ECDL, there are no broad side-lobes visible[4] even though we have lowered the resolution bandwidth from 300 Hz in Fig 49a) down to 30 Hz in Fig 49b).

As the disturbance attenuation $S(s)$ of both loops was quite comparable, this indicates that the frequency noise PSD of the free-running Ti:Sa is much lower than that of the ECDL at offset frequencies above a few kilohertz, which verifies our expectations based on theory (see Fig. 7).

---

[4]In fact, the noise at offset frequencies more than 100 kHz away from the carrier was so low that it was below the noise floor of the spectrum analyzer and therefore proved hard to measure. We are currently investigating ways to improve the signal-to-noise ratio of the measurement and have also gotten our hands on a dedicated phase noise analyzer.

# 6  Summary and Outlook

In this project, we successfully locked various lasers to optical cavities using the PDH technique.

In first step, we stabilized four diode lasers to low-finesse cavities in order to counteract the slow frequency drifts of the free-running lasers over long timescales.

Next, we stabilized two diode lasers and a Ti:Sa laser each to their own high-finesse cavity[5]. As the goal was to not only counteract slow drifts but to also perform linewidth-narrowing, these feedback loops have to be fast. Using closed-loop characterization measurements, we determined time delays to be the main factor limiting the currently achievable loop bandwidth. For the Ti:Sa laser we additionally found piezo-acoustic resonances of its intra-cavity EOM to pose difficulties for control design. Lastly, we performed crude preliminary characterizations of the phase noise of the locked lasers, focusing particularly on their high-frequency noise. As expected, the Ti:Sa featured much less high-frequency noise.

Informed by these characterization measurements, we have decided to focus our further efforts on the Ti:Sa laser for now. By moving the laser into the acoustic enclosure also housing the high finesse cavity it is locked to, we should be able to build a "safe and fast" lock with a bandwidth of a few Megahertz that can mitigate the troublesome EOM resonances. As the noise of the free-running Ti:Sa laser is expected to be small above the relaxation frequency of around $100\,\mathrm{kHz}$, the resulting laser system should allow us to implement single and two-qubit gates free from excess errors due to laser noise. The work towards building this revised system is now already well underway[6].

Once the revised system is up and running, we intend to perform detailed measurements of its phase noise and compare it to that of the other two systems based on diode lasers. This will be greatly facilitated by having the three narrow-linewidth laser systems that were built as part of this thesis: We can perform comparisons between pairs of lasers, and then back out the phase noise of the individual lasers using a so-called three-cornered hat measurement.

---

[5]One of the diode laser systems has been used to successfully perform basic operations with ions in our ion trap, enabling basic characterizations of it.

[6]Just before handing in the final version of this thesis, we successfully managed to implement the envisioned "fast and safe" control design with a gain crossover frequency of about 2 MHz, thus verifying the design considerations above.

# References

[1] Nitzan Akerman et al. "Universal gate-set for trapped-ion qubits using a narrow linewidth diode laser". In: *New Journal of Physics* 17.11 (Nov. 2015), p. 113060. DOI: 10.1088/1367-2630/17/11/113060. URL: `https://dx.doi.org/10.1088/1367-2630/17/11/113060`.

[2] J. Alnis et al. "Subhertz linewidth diode lasers by stabilization to vibrationally and thermally compensated ultralow-expansion glass Fabry-Pérot cavities". In: *Physical Review A* 77 (2008). URL: `10.1103/PhysRevA.77.063809`.

[3] P. et al. Barton. "Measurement of the lifetime of the 3d 2D5/2 state in 40Ca+". In: *Physical Review A 62, 032503* (2000).

[4] J. Bechhoefer. *Control Theory for Physicists*. 2021. Chap. 3. URL: `doi:10.1017/9780511734809.003`.

[5] Eric D. Black. "An introduction to Pound–Drever–Hall laser frequency stabilization". In: *American Journal of Physics* (Jan. 2001). URL: `https://doi.org/10.1119/1.1286663`.

[6] J. I. Cirac and P. Zoller. "Quantum Computations with Cold Trapped Ions". In: *Phys. Rev. Lett.* 74 (20 May 1995), pp. 4091–4094. DOI: 10.1103/PhysRevLett.74.4091. URL: `https://link.aps.org/doi/10.1103/PhysRevLett.74.4091`.

[7] M.L. et al. Day. "Limits on atomic qubit control from laser noise". In: *npj Quantum Inf* 8 (2022). URL: `https://doi.org/10.1038/s41534-022-00586-4`.

[8] Gianni Di Domenico, Stéphane Schilt, and Pierre Thomann. "Simple approach to the relation between laser frequency noise and laser line shape". In: *Appl. Opt.* 49.25 (Sept. 2010), pp. 4801–4807. URL: `https://opg.optica.org/ao/abstract.cfm?URI=ao-49-25-4801`.

[9] Mark Fox. *Quantum Optics: An Introduction*. 2006. Chap. 10.1.

[10] Qubig GmbH. *Test Data Sheet: Resonant electro-optic phase modulator with thermal crystal mount*. English. Version PM7 - VIS. 2017. 4 pp.

[11] Masaharu Hyodo, Kazi Sarwar Abedin, and Noriaki Onodera. "Generation of millimeter-wave signals up to 70.5 GHz by heterodyning of two extended-cavity semiconductor lasers with an intracavity electro-optic crystal". In: *Optics Communications* 171.1 (1999), pp. 159–169. ISSN: 0030-4018. DOI: `https://doi.org/10.1016/S0030-4018(99)00531-3`. URL: `https://www.sciencedirect.com/science/article/pii/S0030401899005313`.

[12] J. Jin and D. A. Church. "Precision lifetimes for the Ca+ 4p 2P levels: Experiment challenges theory at the 1 percent level". In: *Physical Review Letters* 3213–3216 (1993).

[13]    Lintao Li et al. "Active Cancellation of Servo-Induced Noise on Stabilized Lasers via Feedforward". In: *Phys. Rev. Appl.* 18 (6 Dec. 2022), p. 064005. DOI: `10.1103/PhysRevApplied.18.064005`. URL: `https://link.aps.org/doi/10.1103/PhysRevApplied.18.064005`.

[14]    M Squared Lasers Ltd. *Narrow Linewidth, Tunable CW Ti:Sapphire Laser User Manual v10.3.*

[15]    MOGLabs. *External Cavity Diode Laser User Manual.* URL: `https://www.moglabs.com/products/littrow-lasers/MOGLabs_LDL_manual_rev207.pdf`.

[16]    Haim Nakav et al. "Effect of fast noise on the fidelity of trapped-ion quantum gates". In: *Phys. Rev. A* 107 (4 Apr. 2023), p. 042622. DOI: `10.1103/PhysRevA.107.042622`. URL: `https://link.aps.org/doi/10.1103/PhysRevA.107.042622`.

[17]    Robin Oswald. *Characterization and control of a cryogenic ion trap apparatus and laser systems for quantum computing.* PhD Thesis. 2023.

[18]    R. Paschotta. *Finesse.* URL: `https://www.rp-photonics.com/finesse.html`.

[19]    R. Paschotta. *Free spectral range.* URL: `https://www.rp-photonics.com/free_spectral_range.html`.

[20]    R. Paschotta. *Tapered Amplifiers.* URL: `https://www.rp-photonics.com/tapered_amplifiers.html`.

[21]    P. W. Shor. "Algorithms for Quantum Computation: Discrete Logarithms and Factoring". In: *in Proceedings of the 35th Annual Symposium on Foundations of Computer Science* (1994).

[22]    TOPTICA. *DL pro: Tunable diode laser available with digital control DLC pro.* URL: `https://www.toptica.com/index.php?id=60`.

# ETH

Eidgenössische Technische Hochschule Zürich
Swiss Federal Institute of Technology Zurich

## Declaration of originality

The signed declaration of originality is a component of every semester paper, Bachelor's thesis, Master's thesis and any other degree paper undertaken during the course of studies, including the respective electronic versions.

Lecturers may also require a declaration of originality for other written papers compiled for their courses.

I hereby confirm that I am the sole author of the written work here enclosed and that I have compiled it in my own words. Parts excepted are corrections of form and content by the supervisor.

**Title of work** (in block letters):

Laser Stabilization for Manipulation of 40Ca+ Ions

**Authored by** (in block letters):
*For papers written by groups the names of all authors are required.*

**Name(s):**

Cui

**First name(s):**

Yingying

With my signature I confirm that
- I have committed none of the forms of plagiarism described in the 'Citation etiquette' information sheet.
- I have documented all methods, data and processes truthfully.
- I have not manipulated any data.
- I have mentioned all persons who were significant facilitators of the work.

I am aware that the work may be screened electronically for plagiarism.

**Place, date**

Zurich, 30 May 2023

**Signature(s)**

*Yingying Cui*

*For papers written by groups the names of all authors are required. Their signatures collectively guarantee the entire content of the written paper.*